

MXDFz4.4: A LyC emitter 250 Myr after the epoch of reionization and a first test of Ly α morphology as a tracer of LyC escape at high redshift

ILIAS GOOVAERTS ¹, MARC RAFELSKI ^{1,2}, ALEXANDER BECKETT³, GRECCO OYARZÚN ^{4,2}, ANNALISA CITRO ⁵, FARHANUL HASAN ¹, KALINA V. NEDKOVA ⁶, CALUM HAWCROFT¹, ANTON M. KOEKEMOER¹, MITCHELL REVALSKI ¹, MATTHEW J. HAYES ⁷, CLAUDIA SCARLATA⁵, RAY A. LUCAS ¹, NORMAN A. GROGIN ¹, DAVID V. STARK ^{1,2}, PAOLO SUIN ⁸, AND NOR PIRZKAL¹

¹Space Telescope Science Institute, 3700 San Martin Drive, Baltimore, MD 21218, USA

²Department of Physics and Astronomy, Johns Hopkins University, Baltimore, MD 21218, USA

³Aix Marseille Université, CNRS, CNES, LAM (Laboratoire d'Astrophysique de Marseille), 13388 Marseille, France

⁴Homer L. Dodge Department of Physics and Astronomy, The University of Oklahoma, 440 W. Brooks St., Norman, OK 73019, USA

⁵Minnesota Institute for Astrophysics, School of Physics and Astronomy, University of Minnesota, 316 Church Street SE, Minneapolis, MN 55455, USA

⁶IPAC, Mail Code 314-6, California Institute of Technology, 1200 E. California Blvd, Pasadena, CA 91125, USA

⁷Stockholm University, Department of Astronomy and Oskar Klein Centre for Cosmoparticle Physics, AlbaNova University Centre, SE-10691, Stockholm, Sweden

⁸Université Paris-Saclay, Université Paris Cité, CEA, CNRS, AIM, 91191 Gif-sur-Yvette, France

ABSTRACT

Assessing the contribution of ionizing sources to cosmic reionization is a central goal of extragalactic astrophysics. Understanding and quantifying ionizing escape remains challenging near the epoch of reionization. We present the highest-redshift Lyman continuum (LyC) emitter detected to date, MXDFz4.4, at $z = 4.442$ in the MUSE eXtremely Deep Field, observed only ~ 0.25 Gyr after the end of reionization. A high-confidence Ly α line confirms the redshift. LyC flux is detected at 10.3σ in the F435W filter with a flux of 4.2 ± 0.5 nJy, corresponding to a flux measurement at 8.0σ . After correcting for the intrinsic production of LyC photons and the IGM opacity at $z = 4.44$, we derive high escape fractions, f_{esc} , ranging from 50 – 100%. We apply established low-redshift tracers of LyC escape and, for the first time at this redshift, promising Ly α morphological tracers such as the halo fraction. SED fitting indicates the presence of a recent burst of star formation; we explore its impact on the production and escape of ionizing photons. Ly α -based tracers of f_{esc} reveal a complex scenario in which the recent burst strongly influences LyC production and escape, combined with a more evolved stellar population. This interpretation is supported by UV diagnostics, including Σ_{SFR} and sSFR. Our results provide cautious support for the Ly α halo fraction as a LyC escape tracer at high redshift. Considering the burst-driven enhancement in ionizing photon production and escape, we conclude that stochastic star formation in the early universe likely plays a significant role in the contribution of galaxies to cosmic reionization.

Keywords: Galaxies (573), Reionization (1383), Lyman-alpha galaxies (978), Starburst Galaxies (1570)

1. INTRODUCTION

The contribution of ionizing sources to the process of cosmic reionization is a central topic of extra-galactic astrophysics and a key goal of the JWST mission. With the first years of JWST data, significant progress has been made in two of three necessary quantities to con-

strain this contribution: the star formation rate (SFR) density and the production of ionizing photons (per unit SFR). The UV luminosity function (LF) has been robustly constrained up to $z \sim 13$ with photometry (C. T. Donnan et al. 2024; S. L. Finkelstein et al. 2024; Y. Asada et al. 2025) and spectroscopy (Y. Harikane et al. 2024). Integrating these UV LFs gives the SFR density during the epoch of reionization (EoR). The production of ionizing photons has equally been quantified with ex-

cellent statistics by recent works (C. Simmonds et al. 2023; A. Pahl et al. 2025; M. Llerena et al. 2025; M. J. Hayes et al. 2025), finding either slight or no redshift evolution.

However the third necessary quantity, the escape fraction of ionizing photons, f_{esc} , remains elusive. Ionizing flux cannot be directly observed in the EoR, due to absorption of ionizing photons by the intervening neutral HI gas in the inter-galactic medium (IGM). Therefore f_{esc} must be understood at lower redshifts and indirect tracers established, which we can use to quantify the escape of ionizing photons within the EoR. Significant progress has been made in recent years at low- z , principally by the Low- z Lyman Continuum Survey (LzLCS: S. R. Flury et al. 2022a, see also J. Chisholm et al. 2022; A. Le Reste et al. 2025), which has studied in detail 35 Lyman continuum emitters (LCEs) at $z \sim 0.3$, but also in a number of other studies (Y. I. Izotov et al. 2016; A. Verhamme et al. 2017; Y. I. Izotov et al. 2020, 2022, 2024b, see A. E. Jaskot 2025 for a review). The most important findings are that Ly α properties, such as equivalent width (EW) and escape fraction, $f_{esc, Ly\alpha}$, correlate well with f_{esc} (A. Henry et al. 2015; A. Verhamme et al. 2017; C. C. Steidel et al. 2018; S. R. Flury et al. 2022b), while line separation from systemic redshift and halo fraction show a strong anti-correlation with f_{esc} (A. Verhamme et al. 2015; Y. I. Izotov et al. 2018b, 2020; S. R. Flury et al. 2022b; A. Saldana-Lopez et al. 2025). Combined, these results connecting Ly α and LyC emission highlight the importance of clear channels (low HI column density) in the interstellar medium of the host galaxy in allowing Lyman photon escape.

Other galaxy properties that have been found to correlate well with f_{esc} include SFR surface density, Σ_{SFR} (Y. I. Izotov et al. 2016; E. Vanzella et al. 2018; S. R. Flury et al. 2022b; A. E. Jaskot et al. 2024), blue UV slopes (β , J. Chisholm et al. 2022; Z. Ji et al. 2025), a high [O III]/[O II] ratio (Y. I. Izotov et al. 2018b, 2020; A. E. Jaskot et al. 2024) and the presence of strong UV lines such as CIV $\lambda 1550$ (D. Schaerer et al. 2022; A. Saxena et al. 2022; Y. I. Izotov et al. 2024a). High Σ_{SFR} is a likely contributing factor to the creation of the clear channels crucial to LyC escape and the correlation with low β values is attributed to the role of dust in blocking LyC photons. High [O III]/[O II] ratios in LCEs has been attributed to feedback from massive stars as well as the ratio’s sensitivity to ionization parameter.

However, no single tracer alone reliably predicts the escape of ionizing photons, underscoring the need for a framework which predicts the escape of LyC photons from all available tracers, as well as an assessment of the most important variables for tracking the escape of LyC

photons, such as in M. Maji et al. (2022); A. E. Jaskot et al. (2024). We have reached the point at low redshift that such multivariate predictors can be used on the appreciable sample of LCEs collated in the literature. It is additionally possible to apply such techniques to simulated data (J. Rosdahl et al. 2022; N. Choustikov et al. 2024). However, due to a lack of data as comprehensive as the LzLCS for a statistically significant population $z > 2$, we are not yet at this stage at high-redshift.

At $z > 2$, which we term “high redshift” for the purposes of this work, there remain a number of open questions. Recent studies have cast doubt on the ability of Ly α properties to reliably trace f_{esc} at high- z (M. J. Rutkowski et al. 2017; J. Kerutt et al. 2024; A. Citro et al. 2025). A. Citro et al. (2025) found galaxies with strong Ly α emission but without traces of LyC emission at the expected strength based on low- z estimators. J. Kerutt et al. (2024) found a diversion from the well-established relation at low redshift between f_{esc} and Ly α peak separation (Y. I. Izotov et al. 2018b), and high scatter around the well-established Ly α EW and f_{esc} relation (C. C. Steidel et al. 2018).

Therefore, doubts persist over the applicability of low-redshift f_{esc} tracers during the EoR, which is their primary purpose. As ~ 12 Gyr of evolution has taken place between the EoR and our low-redshift measurements, there are numerous factors which may influence the universal validity of f_{esc} tracers, for example the merger fraction, known to increase with redshift (V. Rodriguez-Gomez et al. 2015), the evolution of the star formation efficiency (P. Madau et al. 1996) and the UV background (X. Fan et al. 2006). It is therefore important to search for LCEs as close to the EoR as possible, in order to assess low redshift tracers in the epoch where they become cosmologically relevant.

In this work, we describe the detection of an LCE at $z = 4.442$, within ~ 0.25 Gyr of the EoR, in the MUSE eXtremely Deep Field (MXDF; R. Bacon et al. 2023), which we henceforth refer to as MXDFz4.4. MXDFz4.4 has a 10.3σ detection in the HST/ACS F435W filter which probes wavelengths blueward of 912 \AA with a redshift confirmed by a high-confidence, asymmetric Ly α emission line in the MUSE data. In §2 we describe the MUSE data used to detect the Ly α line, as well as the HST and JWST data used to detect the LyC flux and spectral energy distribution (SED) of the galaxy. §3 describes MXDFz4.4 and the necessary modeling to derive its properties, primarily f_{esc} : SED fitting and modeling of IGM transmission. We then evaluate all accessible f_{esc} tracers which have been established at low redshift, focusing on the important Ly α -LyC connection in §5. Finally we interpret this discovery in relation

to the transmission of the IGM and the properties of MXDFz4.4 and offer conclusions in §6 and §7.

Throughout this paper, we adopt a value for the *Hubble* constant of $H_0 = 70 \text{ km s}^{-1} \text{ Mpc}^{-1}$, and the cosmology used is $\Omega_\Lambda = 0.7$ and $\Omega_m = 0.3$. All IMFs used are stated throughout the text and magnitudes are given in the AB mag system (J. B. Oke & J. E. Gunn 1983). All equivalent widths are given in the rest frame unless otherwise stated.

2. THE MUSE EXTREMELY DEEP FIELD

The MUSE eXtremely Deep Field (MXDF; GTO Program 1101.A-0127, PI R. Bacon, R. Bacon et al. 2023) is a region of extremely deep observations by the MUSE integral field spectrograph on the VLT, with the deepest area having a total exposure time of 141h. MUSE has a field of view of $1 \times 1'$ with a spatial pixel size of $0''.2$, and a spectral range of $4700 - 9350 \text{ \AA}$ with a spectral pixel size of 1.25 \AA . This allows it to detect Ly α emission in the redshift range $2.9 < z < 6.7$. All MXDF data is publicly available⁹ and viewable using the web interface¹⁰.

The MXDF is situated within the footprint of the Hubble Ultra Deep Field (HUDF; S. V. W. Beckwith et al. 2006), with additional public HST ACS/WFC and WFC3/UVIS imaging contributed from programs including GOODS (M. Giavalisco et al. 2004), CANDELS (N. A. Grogin et al. 2011; A. M. Koekemoer et al. 2011), 3D-HST (G. B. Brammer et al. 2012), UVCANDELS (X. Wang et al. 2025), UVUDF (H. I. Teplitz et al. 2013), and HDUV (P. A. Oesch et al. 2018). The HST filters used in this analysis are WFC3/UVIS F336W, and ACS/WFC F435W, F606W, F775W, F814W, and F850LP. The F435W filter, in which MXDFz4.4's LyC emission is detected, has an average depth of 150 ks. The latter data have been reprocessed as part of HST archival program PID 16621 (PI: Koekemoer), including calibration improvements from updated darks, biases, flatfields and astrometric alignment, as well as other low-level improvements including improved removal of cosmic rays, satellite trails, and bad pixels.

This field also benefits from public JWST imaging from the JADES and JEMS programs (D. J. Eisenstein et al. 2023; M. J. Rieke et al. 2023; C. C. Williams et al. 2023), where the JWST/NIRCam filters from these programs that we use are: F090W, F115W, F150W, F182M, F200W, F210M, F277W, F335M, F356W, F410M, F430M and F444W. F460M and F480M are also included in the JADES imaging data release (M. J. Rieke

et al. 2023), however we elect not to include these filters in our analysis, as they have a low SNR, which likely results in underestimated photometric uncertainties.

2.1. Photometry of MXDFz4.4

We perform custom photometry on the full-resolution images to maximize the resulting flux SNR of MXDFz4.4. The segmentation map released by the JADES collaboration blends MXDFz4.4 with a faint neighbor to the southeast so we create a custom version where these sources are carefully de-blended. We perform Kron photometry (R. G. Kron 1980) on the full-resolution images, and correct these values by 10%, consistent with curve-of-growth analysis checks we performed. We note that the neighbor is very faint so this has minimal effects on the photometry published in M. J. Rieke et al. (2023).

As the emission in F435W is spatially far more compact than in redder filters, we apply a different method to maximize the SNR in this filter, similar to that used by M. Rafelski et al. (2015); L. Sun et al. (2024) for faint UV photometry of the UVUDF and UVCANDELS surveys. Specifically, we calculate an isophotal flux using a segmentation map based on the F606W filter, a neighboring filter where MXDFz4.4 is more compact than the detection image used by JADES, but still high enough SNR to create a reliable segmentation map. This smaller aperture fully captures the flux in the F435W filter and reduces contribution from sky dominated pixels, thereby increasing the SNR of the flux measurements.

We connect the F435W flux to the rest of the photometry using an aperture correction based on the larger JADES-based isophotal area. This correction is determined by taking the ratio of the isophotal flux measured in the smaller and larger isophotal areas in the F606W image. This correction assumes that the distribution of flux is similar in F606W and F435W, which is confirmed both visually and by comparison of the F435W flux measured in the larger isophotal area. The two flux measurements agree within the smaller isophotal area uncertainties as expected. This F606W isophotal area flux measurement is then used to define the SNR of the detection. The F435W detection significance is 10.3σ .

We correct for the effects of the point spread function (PSF) by applying published encircled energy corrections (similar to PSF matching) to the resultant Kron photometry, which is reasonable given the compactness

⁹ <https://amused.univ-lyon1.fr>

¹⁰ <https://amused.univ-lyon1.fr/project/UDF/browse>

of our galaxy¹¹¹². The alternative standard method of PSF matching the images before measuring the photometry would reduce the SNR of the F435W photometry, as it would smooth the flux over the larger F444W PSF and thus increase our flux uncertainty. We confirm the validity of this method in two ways. First, we check the curves of growth of the photometry including the encircled energy correction and find convergence at large radii. Second, we compare the photometry of the redder HST and JWST photometry with this method to that of the PSF matched photometry from JADES and find good agreement. Therefore this Kron flux corrected to the total flux (10%) plus the encircled energy correction is used as our final flux measurement, and we propagate the uncertainties from each correction. The resultant LyC flux measurement in F435W is 4.2 ± 0.5 nJy, at 8.0σ . We subsequently use this photometry for the SED fitting described in §3.1.

2.2. Spectral Extraction of MXDFz4.4 from the MXDF datacube

The MUSE consortium makes their spectra public, the extraction of which follows R. Bacon et al. (2023). We briefly outline this procedure here, specifically that which relates to extraction using the ORIGIN software (D. Mary et al. 2020), as this is the method used for MXDFz4.4. The ORIGIN software is optimized to detect faint line emitters in MUSE datacubes. Care is taken to mask any bright continuum sources in a three-stage process. The first two stages involve segmenting and masking out any bright, noisy sources, firstly on the datacube itself, creating a white light continuum image, then on the S/N residual image thereof. Principal Component Analysis is then used iteratively to clean further residuals from each spaxel in the cube. Emission lines are then detected by filtering the datacube with possible spectral line profiles. Each source is then extracted from the original datacube using the algorithm from K. Horne (1986). These extracted spectra are publicly available for all line-emitters detected in the MXDF. We take the spectrum for MXDFz4.4 and apply a custom fitting process which is described in Sect. 5.1.1. This process also follows the line-fitting procedure for Ly α lines described in R. Bacon et al. (2023) but allows us to extract and visualize all necessary Ly α properties.

¹¹ HST: <https://www.stsci.edu/hst/instrumentation/acs/data-analysis/aperture-corrections>

¹² JWST: <https://jwst-docs.stsci.edu/jwst-near-infrared-camera/nircam-performance/nircam-point-spread-functions#NIRCamPointSpreadFunctions-Encircledenergiesforresampleddata>

3. MXDFz4.4

The LyC emitter, which we dub MXDFz4.4, is located in the deepest section of the MXDF (exposure time ~ 140 hrs) at an RA and DEC of 53.1577218, -27.7822649 , and a redshift (from the Ly α emission line) of 4.442. This makes it the highest-redshift directly-observed LCE to date, located within ~ 0.25 Gyr of the end of the EoR.

MXDFz4.4 has an observed ratio of ionizing to non-ionizing flux, $\frac{F_{\text{LyC}}}{F_{1500}}$ (in F_ν units), of 0.18 ± 0.03 , calculated from the F435W to F775W flux ratio. We adopt the nomenclature F_{LyC} to denote the LyC flux detected in F435W, rather than F_{900} to differentiate from studies where the flux at exactly 900 Å is used from spectra. The F435W band covers up to 900 Å rest frame, but starts below 700 Å so we term this wavelength range “LyC”.

The LyC escape fraction, f_{esc} , values that we derive, depending on the intrinsic ratio of ionizing to non-ionizing flux, as well as IGM attenuation, are presented in Table 1, and discussed in §4. The properties of MXDFz4.4, derived from SED fitting are detailed in §3.1, as well as detailed analysis of the Ly α emission line observed by MUSE in §5.1. The HST and JWST imaging of MXDFz4.4 is shown in Fig. 1 and the MUSE spectrum is shown in Fig. 2.

While the spectrum shows only one emission line, MXDFz4.4 has a confident redshift as the line has an asymmetric profile, typical of Ly α emission lines. We include a detailed discussion how we rule out other possible redshifts in Appendix A. No lines other than Ly α are detected in the spectrum. There is a spectrum of MXDFz4.4 using JWST NIRISS Wide-Field slitless spectroscopy from NGDEEP (PID 2079; PIs: S. Finkelstein, C. Papovich, N. Pirzkal, M. B. Bagley et al. 2024), however there are no lines detected. This is also to be expected; we show the spectrum and offer a full explanation in Appendix B.

3.1. SED fitting

We use the CIGALE SED fitting code to derive MXDFz4.4’s properties, fitting the observed photometry with a flexible, non-parametric star formation histories (SFH). We do not fit with the IGM-affected bands, F606W and F435W, in order to predict the ratio of UV to ionizing photons, L_{1500}/L_{LyC} , which we require to calculate the intrinsic escape fraction of MXDFz4.4 (see §4). As mentioned in §2, we also do not fit the F460M and F480M bands. We fit using two different stellar population synthesis models to assess the impact that this choice has on the derived properties.

The CIGALE SED fitting code (D. Burgarella et al. 2005; M. Boquien et al. 2019) builds composite stellar

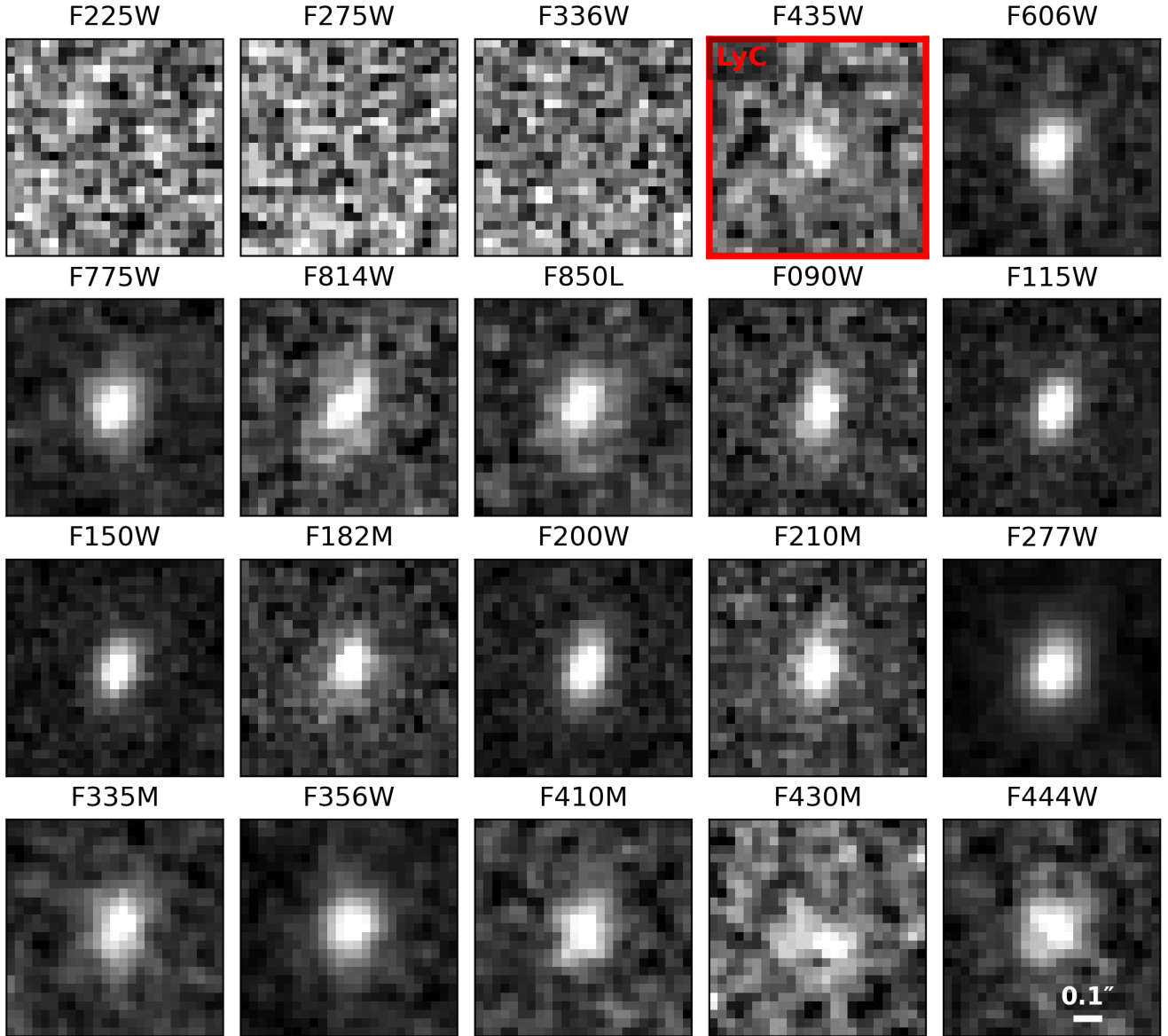


Figure 1. Cutouts of MXDFz4.4 in all filters used for SED fitting, as well as F225W, F275W and F336W to show non-detections. The reduction of the HST data is outlined in Sect. 2 and the remaining (JWST) filters are from the JADES program (M. J. Rieke et al. 2023). All filters have a pixel scale of $0''.03$. The LyC flux in F435W, at 8.0σ significance, is clearly visible.

populations based on a flexible star-formation history by combining stellar population models from G. Bruzual & S. Charlot (2003) (henceforth BC03) and BPASS v2.2 J. J. Eldridge et al. (2008, 2017). The BPASS models are able to include the effects of binary populations on stellar evolution. Switching these binary effects on or off, as well as switching between the different extinction laws (MW, LMC, SMC) affects the best fit galaxy properties, including the intrinsic L_{1500}/L_{LyC} , without a significant change in the reduced chi-squared of the fit. We therefore run CIGALE using the BPASS models in each of these cases (making six separate runs) and measure the galaxy properties. The range of values spanned by these

runs therefore provides a more realistic uncertainty on each measurement than the uncertainty calculated from a single run of CIGALE.

CIGALE also accounts for gas ionized by massive stars, as well as extinction and re-emission due to dust using a modified D. Calzetti et al. (2000) extinction law. We use a Chabrier IMF (G. Chabrier 2003) and adopt a non-parametric SFH with 10 bins covering the past 600 Myr. The latest bin covers the most recent 5 Myr, with the remaining bins equally-sized in log space. The best-fit is found with an SFH that remains very low until ≈ 10 Myr before the galaxy is observed, rising into a strong burst in the most recent 5 Myr. The resulting model can be

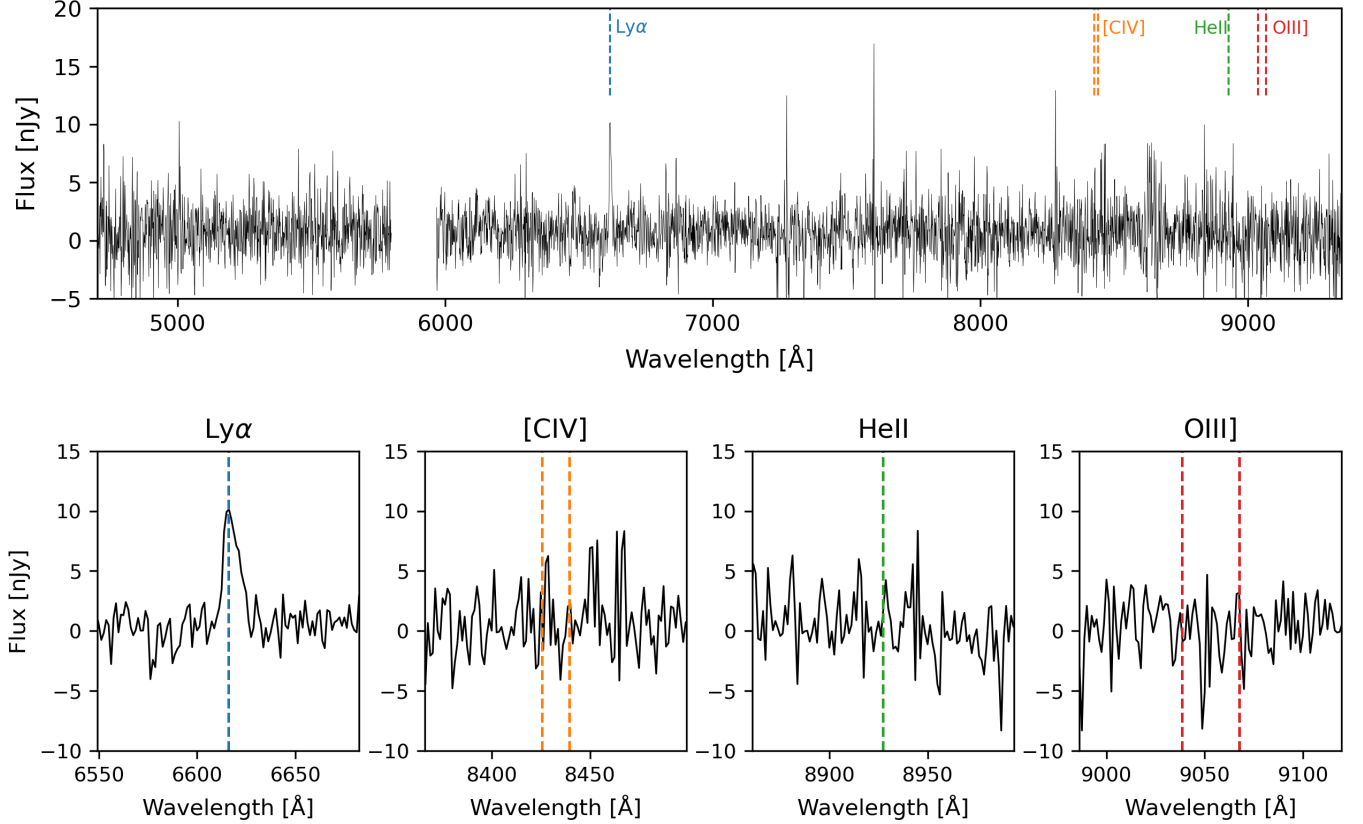


Figure 2. MUSE spectrum of MXDFz4.4. Cutouts of the UV lines are shown enlarged below the main spectrum. The Ly α line at 6615.9 Å is evident from its asymmetric line shape. No other emission lines are detected in the MUSE spectrum.

used to predict the intrinsic emission in the LyC regime. We derive values of 1.01 ± 0.24 and $1.0 - 1.2$ for the BC03 models and BPASS respectively, by convolving the resulting best fit spectra with the F435W and F775W filter transmissions. We note that using a ‘delayed-tau’ SFH model returns very similar results; the best fit is found with a strong burst ≈ 5 Myr in the past. The best fits using the BC03 and BPASS models (with the non-parametric SFH) are shown in Fig. 3. All SED fitting-derived results, including derived escape fractions (see also §4), are given in Table 1. Quantities derived using the BPASS models are given as a range, encompassing the values derived during all runs.

The SFH derived from CIGALE shows a recent ($\lesssim 10$ Myr) burst of intense star formation in MXDFz4.4. Due to the likely impact of this recent burst on f_{esc} (due to stellar feedback clearing holes in the ISM; M. Trebitsch et al. 2017; D. Rahner et al. 2017; C. A. Carr et al. 2025), we additionally consider L_{1500}/L_{LyC} values taken directly from two different stellar population synthesis models of young stars ($\lesssim 10$ Myr), BPASS (J. J. Eldridge et al. 2008) and the recent pySTARBURST99 models (C. Hawcroft et al. 2025). Both of these codes incorporate effects that can be significant for the pro-

duction of LyC photons. pySTARBURST99 includes the effects of stellar rotation as well as very massive stars (VMS), up to $300 M_{\odot}$ (see Fig. 4). BPASS takes into account the effect of binary populations. Additionally, CIGALE may struggle to fit a very young population due to a sparsity of very young star templates, additionally motivating an analysis using these specialized stellar models. Both population synthesis codes utilize a similar framework to make predictions of synthetic observables based on grids of input stellar evolution models and spectral libraries. The key differences are that BPASS accounts for binary stars in the stellar evolution models, while pySTARBURST99 includes the impact of rotation. The codes also use different stellar libraries, however the only significant difference should be that pySTARBURST99 includes synthetic spectra of VMS which can reduce the L_{1500}/L_{LyC} ratio while BPASS extrapolates these from a regular OB grid (relevant in the first ~ 3 Myr). In Fig. 4 we show the evolution of L_{1500}/L_{LyC} over the first 10 Myr for a range of metallicities, including the effects of VMS. The L_{1500}/L_{LyC} from CIGALE is consistent with the range shown, which supports the idea of a very recent burst in MXDFz4.4. Additionally, we show the escape fractions derived us-

Table 1. Escape fraction of MXDFz4.4 and SED-fitting derived properties

f_{LyC}/f_{1500}	L_{1500}/L_{LyC}	T_{IGM}	$f_{\text{esc}}^{\text{rel}} [\%]$	A_v	$f_{\text{esc,abs}}^{\text{IGM}} [\%]$
0.18 ± 0.03	3^a	0.18	300%	$0.34^b - 0.68^c$	160 – 220
	1.0-1.5 ^d	0.18	100 – 150%	$0.34^b - 0.68^c$	53 – 109
	1.01 ± 0.24^b	0.18			100 ± 15
	1.0-1.2 ^c	0.18			100 – 120

M_{UV}	SFR ₁₀ [M_{\odot}/yr]	SFR ₁₀₀ [M_{\odot}/yr]	M_{\star} [M_{\odot}]
-20.1 ± 0.1	11.8 ± 0.6^b	2.4 ± 0.1^b	$10^{8.3 \pm 0.2^b}$
	1.4 – 3.3 ^c	0.29 – 1.2 ^c	$10^{7.5-8.0^c}$

^aValue from literature.

^bValue from fitting with BC03 models (G. Bruzual & S. Charlot 2003).

^cValue from fitting with BPASS models (J. J. Eldridge et al. 2017).

^dValue from pySTARBURST99 models (C. Hawcroft et al. 2025).

NOTE—A table of MXDFz4.4’s properties related to escape fraction and properties of the host galaxy derived from SED fitting with CIGALE (see text). The upper table pertains to escape fraction properties, with the first two rows using luminosity ratios derived from stellar population models, a value commonly assumed in the literature, 3 (C. C. Steidel et al. 2001; J. Kerutt et al. 2024) and the values derived from young, metal-poor pySTARBURST99 models. Both these rows use the range of dust attenuation values derived by our SED fitting with CIGALE. The final escape fractions are given as a range based on the ranges of $f_{\text{esc}}^{\text{rel}}$ and A_v . The bottom two rows use the luminosity ratios directly from CIGALE, which already have dust attenuation included. The luminosity ratio from BPASS is given as a range based on different runs (see §3.1). All these results use a T_{IGM} value of 0.18 (see text). The lower table contains SED fitting-derived properties of the host galaxy, with the first row using the BC03 models and the second row BPASS. BPASS-derived values are given as a range, based on the values derived in all BPASS runs (see text).

ing the luminosity ratios from these models alongside the CIGALE-derived escape fractions in Table 1 We discuss the consequences for MXDFz4.4’s escape fraction in §4 and §6.

3.2. IGM modeling

The IGM is expected to absorb large fractions of ionizing photons at $z \gtrsim 3.5$ (A. K. Inoue 2011; A. K. Inoue et al. 2014). Despite this, LCEs have been confirmed at redshifts up to $z \sim 4$ (E. Vanzella et al. 2018; U. Meštrić et al. 2025) and candidates exist up to $z \sim 4.4$ (L. J. Prichard et al. 2022; J. Kerutt et al. 2024). MXDFz4.4 is the highest-redshift LCE confirmed to date, which makes it imperative to assess whether it is possible to have an IGM sightline transmissive enough to allow us to observe the ionizing flux, or whether the detection of MXDFz4.4 calls into question our models of IGM transmission near the EoR.

We model the IGM using the TAOIST routine described in R. Bassett et al. (2021). In brief, mock sightlines are populated with HI absorbers at randomized locations following the redshift-dependent column density distribution function (CDDF) given by C. C. Steidel et al. (2018). We model individual HI absorbers with column densities between 10^{12} and 10^{21} cm^{-2} which, at wavelengths redder than 912 Å, produce Voigt pro-

files with varying Doppler widths (sampled from L. Hui et al. 1999). At bluer wavelengths, the absorption cross-section is proportional to λ^3 (D. E. Osterbrock 1974). By integrating the transmission curve through our LyC band, we can calculate the transmission of the IGM (T_{IGM}), the fraction of flux in F435W that would pass through the IGM along that mock sightline.

In order to adequately sample the T_{IGM} distribution, we produce 10,000 mock sightlines. The TAOIST code allows for a different CDDF in the CGM of the galaxy, where the higher gas density leads to more high-column-density absorbers. As the redshift of MXDFz4.4 is based on the Ly α line, it is not clear whether there is Ly α emission at the systemic redshift. We therefore produce two sets of mock sightlines, one including absorption from the CGM of MXDFz4.4, the other assuming a clear channel through the CGM along which Ly α and LyC photons can escape. The T_{IGM} distribution from both sets of sightlines is shown in Figure 5. Given that MXDFz4.4 must be in a sightline with higher than average transmission, we select the 3σ value from our list of modeled sightlines for use in deriving our escape fractions; $T_{\text{IGM}} = 0.18$.

The CDDF used in this modeling was produced using measured HI absorbers at $2.0 \lesssim z \lesssim 2.8$ (G. C. Rudie et al. 2013), with a power law used to denote the redshift

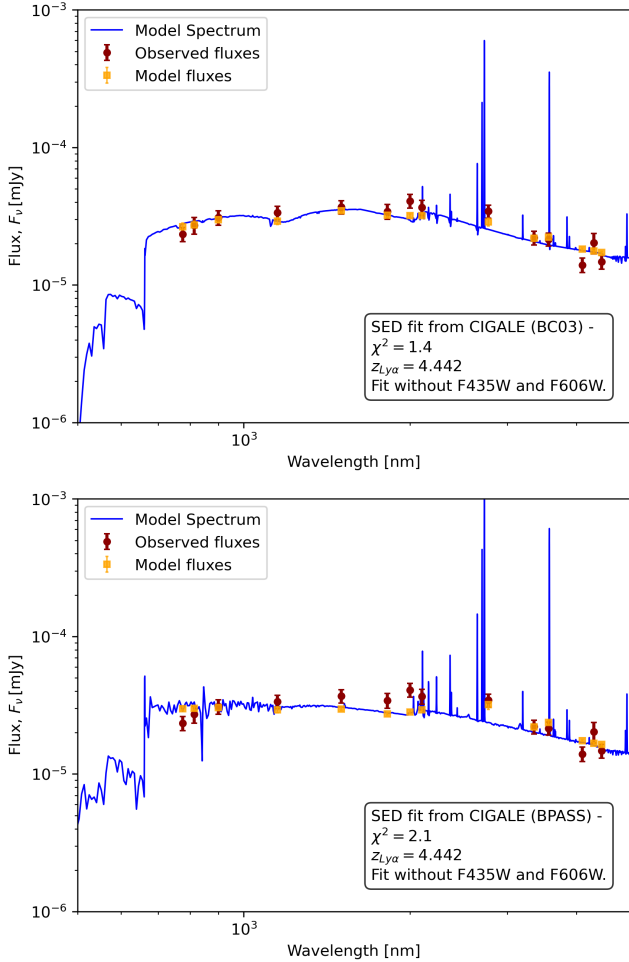


Figure 3. The best fit spectra of MXDFz4.4 from CIGALE using the BC03 and BPASS stellar population models (G. Bruzual & S. Charlot 2003; J. J. Eldridge et al. 2017), plotted in blue. The observations are overplotted in red and model fluxes in orange. The fit was performed without F435W and F606W in order to predict the IGM affected bands and derive L_{1500}/L_{LyC} . The redshift was fixed to the value of $z = 4.442$ as derived from the Ly α emission line.

evolution of the CDDF. Extrapolating this redshift evolution to $z > 4$ may not produce accurate results, as IGM conditions may change close to the EoR. The CDDF also becomes more difficult to measure at low column densities as we consider higher redshifts, as individual absorbers become more difficult to resolve in the Ly α ‘jungle’ (R. M. Bielby et al. 2020). This is particularly important as high-column-density Lyman Limit Systems (LLSs) are expected to dominate the absorption of LyC photons (A. K. Inoue et al. 2014), but the tail of most transparent sightlines will feature fewer LLSs, and hence their transmission will depend on the prevalence of the lower-column-density absorbers. We also note that this simulation does not include the effect of the large scale

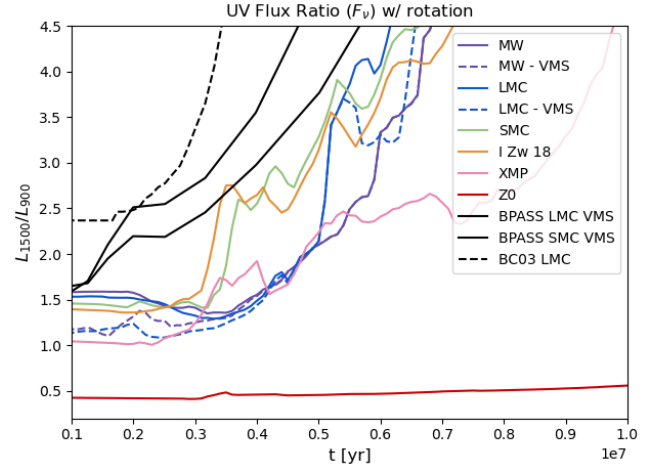


Figure 4. Evolution of L_{1500}/L_{LyC} over the first 10 Myr of a starburst, based on the models from pySTARBURST99 models (in color) (C. Hawcroft et al. 2025) as well as BPASS (J. J. Eldridge et al. 2008, 2017) and BC03 (G. Bruzual & S. Charlot 2003) (in black). Values have been convolved with the F435W and F775W transmission curves and are in F_ν such that they are comparable to the observations. Metallicities range from Milky Way metallicity ($\sim 0.14Z_\odot$) or XMP - extremely metal poor ($\sim 10^{-5}Z_\odot$), with a zero metallicity line included for comparison. VMS indicates models including very massive stars, up to $300 M_\odot$.

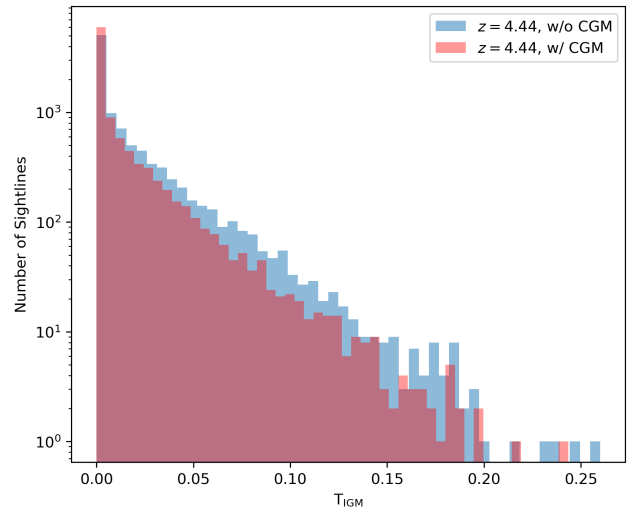


Figure 5. The transmission of the IGM (defined as $e^{\tau_{\text{IGM}}}$) through F435W to the redshift of MXDFz4.4, based on 10,000 mock sightlines modeled using the TAOIST code as described in S3.2. We show the results including and excluding the CGM of MXDFz4.4.

structure which may result in a systematic bias in the estimate of T_{IGM} (C. M. Scarlata et al. 2025).

4. THE ESCAPE FRACTION OF MXDFz4.4

In this section we start by defining the terms used in the explanation and calculation of the LyC escape fraction. This is followed by the measured and derived quantities for MXDFz4.4.

4.1. Escape fraction definitions

The observed flux ratio between the photometric bands which measure the flux bluewards of 912 Å (LyC flux) and UV flux, already presented, is denoted by $f_{\text{LyC}}/f_{\text{UV}}$. This contains no model assumptions and is purely an observed quantity. However, the effect of the absorption by the IGM is not taken into account, neither is the intrinsic ratio between the ionizing and non-ionizing flux. These quantities are captured in the relative escape fraction (C. C. Steidel et al. 2001; B. Siana et al. 2007);

$$f_{\text{esc,rel}} = \left(\frac{f_{\text{LyC}}}{f_{\text{UV}}} \right)_{\text{observed}} \left(\frac{L_{\text{UV}}}{L_{\text{LyC}}} \right)_{\text{intrinsic}} e^{\tau_{\text{IGM}}}. \quad (1)$$

We note that the exponential factor at the end of this expression is equal to T_{IGM} , which is plotted in Fig. 5. Both this and the UV-to-ionizing luminosity ratio are model dependent quantities, the first derived by the TAOIST modelling (§3.2) and the second by our SED fitting (§3.1).

Typically, a further quantity is defined to account for the effect of absorption by dust in the galaxy, termed the absolute escape fraction;

$$f_{\text{esc,abs}}^{\text{IGM}} = f_{\text{esc,rel}} \times 10^{-0.4A_v}, \quad (2)$$

where A_v is the dust attenuation in the rest frame UV, another model-dependent quantity, and we mark this quantity with the superscript IGM to denote that it is corrected for IGM absorption. We present two methods of deriving MXDFz4.4's escape fraction, the first assuming an intrinsic luminosity ratio in Eq. 1 which comes from stellar population models. We then correct for dust using Eq. 2. We use an intrinsic luminosity ratio of 3, common in the literature (C. C. Steidel et al. 2001; J. Kerutt et al. 2024) and a range, 1.0 – 1.5, based on our young, metal-poor pySTARBURST99 models (Fig. 4). The second method derives the luminosity ratio directly from the CIGALE best-fit model (see §3.1), which already takes dust attenuation into account, hence arriving directly at $f_{\text{esc,abs}}^{\text{IGM}}$.

4.2. Escape fraction derivations

Starting from Eq. 1, we measure the flux ratio to be 0.18 ± 0.03 . The second term, the luminosity ratio, derived with CIGALE and depending on the stellar population synthesis models used, is 1.01 ± 0.24 (BC03) and

1.0 – 1.2 (BPASS). The luminosity ratios from the literature and from the pySTARBURST99 models are 3 and 1.0 – 1.5 respectively.

Going forward, we consider that the MXDF is a sightline which has a transmission 3σ above the mean simulated transmission, with $T_{\text{IGM}} \sim 0.18$ (see §3.2). We discuss this assumption, as well as the possibility that the sightline is more, or less transmissive, in §6. This gives us $f_{\text{esc,abs}}^{\text{IGM}}$ values of $100 \pm 15\%$ (BC03) and 100 – 120% (BPASS). Considering a luminosity ratio of 3, and the attenuation derived by our SED fitting, we arrive at an $f_{\text{esc,rel}}$ of 300% and a possible $f_{\text{esc,abs}}^{\text{IGM}}$ range of 160 – 220%. As this results in an escape fraction $\gg 100\%$, we consider it unlikely that the intrinsic luminosity ratio in MXDFz4.4 is as high as 3. This is further discussed in §6.

As mentioned in §3.1, in order to further investigate the low luminosity ratios we derive using SED fitting, we also examine a variety of metallicity and age-dependent luminosity ratios derived from pySTARBURST99 models (C. Hawcroft et al. 2025) (Fig. 4, where they are plotted together with select BPASS and BC03 models). As our SED fitting shows a recent burst in MXDFz4.4's SFH, we consider the first 10 Myr of evolution for these models. The range of L_{1500}/L_{LyC} values given by the BPASS and pySTARBURST99 models is $\sim 1 - \sim 20$ (not including the 0 metallicity population), with the higher-metallicity models predicting $L_{1500}/L_{\text{LyC}} \sim 20$ by an age of 10 Myr. We focus on the low L_{1500}/L_{900} end of this range in Fig. 4 to show the differences between all the models at young ages. The L_{1500}/L_{LyC} value derived from CIGALE is low, in the range shown, so this plot is useful to visualize the possible nature of the recent burst in MXDFz4.4. We discuss this further in §6. The luminosity ratio range we consider from the young pySTARBURST99 stellar models, 1.0 – 1.5 which captures the low-metallicity stellar populations at an age of $\lesssim 5$ Myr. This gives an $f_{\text{esc,rel}}$ range of 100 – 150% and an $f_{\text{esc,abs}}^{\text{IGM}}$ range of 53 – 109%.

As an escape fraction of $> 100\%$ is unphysical, either L_{1500}/L_{LyC} must be below a certain value, or our result invokes a tension with the IGM models described in the previous section. We consider a lower bound of 53%, as given using the luminosity ratios from the pySTARBURST99 models. While a range of $f_{\text{esc}} = 53 - 100\%$ is large in absolute terms, this reflects the uncertainty surrounding the model assumptions inherent to the f_{esc} calculation at high-redshift, where we do not know the intrinsic ratio of ionizing to UV photons, or the exact opacity of the IGM. Moreover, the small number of LCEs in the literature within this range are classed as strong LCEs, making a comparison with MXDFz4.4

useful. This is further discussed in §6. We now move on to comparing the properties of MXDFz4.4 to other objects in the literature and f_{esc} tracers established at low-redshift.

5. EVALUATING f_{esc} TRACERS

As MXDFz4.4 is within ~ 0.25 Gyr of the end of the EoR (S. E. I. Bosman et al. 2022) it represents a unique opportunity to study the f_{esc} tracers established at low redshift (S. R. Flury et al. 2022a; A. E. Jaskot 2025) close to the end of the EoR, where we must eventually apply these relations. The elapsed time between the end of the EoR and the detection redshift of MXDFz4.4 is a factor of ~ 35 less than the local Universe where the aforementioned successful f_{esc} studies were carried out. We note that it is also a factor of 3–4 less than the time between the end of the EoR and $z \sim 3-3.5$, where previous high-redshift f_{esc} studies based on multiple galaxies have been focused (C. C. Steidel et al. 2018; A. J. Pahl et al. 2021; T. E. Rivera-Thorsen et al. 2022; A. Beckett et al. 2025).

This means that MXDFz4.4 represents a significant step forward in measuring the properties of the LCEs actually responsible for the reionization process. First we focus on the important Ly α -LyC connection, taking full advantage of MUSE’s spectral resolution and spatial information. In following sections we also connect the SFR surface density, Σ_{SFR} , and the UV slope with f_{esc} .

As mentioned in the previous section, we consider in our analysis an envelope of possible escape fractions from 53–100%, ranging from the minimum value (based on L_{1500}/L_{LyC} ratios) to the maximum possible value, which is implied by our IGM transmission corrections. While this is a large range in absolute terms, there are few LCEs observed in the local universe with $f_{esc} > 50\%$, hence it remains useful to compare MXDFz4.4’s properties with those LCEs of high escape fraction that have been observed.

5.1. The Ly α -LyC connection

The most promising tracers of f_{esc} at low redshift are the properties of Ly α emission, both spectral and spatial (S. R. Flury et al. 2022b; A. E. Jaskot et al. 2024; A. Saldana-Lopez et al. 2025). Thanks to the IFU data of MXDFz4.4 from MUSE, we have full access to both. In the following sections, we outline the Ly α properties of MXDFz4.4 and establish whether they agree with the predictions from low-redshift for LCEs and therefore what the prospects are for using these predictions within the EoR. A summary of all the relevant properties is given in Table 2.

Table 2. MXDFz4.4 Ly α Properties

Property	Value
Flux	$93 \pm 8 \times 10^{-20}$ erg/s/cm ²
Luminosity	$9.8 \pm 0.8 \times 10^{41}$ erg/s
EW	17 ± 2 Å
FWHM	405 ± 52 km/s
Red peak asymmetry	2.1 ± 0.6
$r_{50, Ly\alpha}$	$2.4^{+0.6}_{-0.5}$ kpc
$f_{esc, Ly\alpha}$	$8 - 38\%^a, 27 - 300\%^b, 13 \pm 2\%^c$
Halo Fraction	$0.27^{+0.15}_{-0.18}$

^aUsing SFR derived from CIGALE using BC03 models.

^bUsing SFR derived from CIGALE using BPASS models. Range comes from range of SFRs derived in different runs (see §3.1).

^cDerived using UV magnitude observed in F775W filter.

NOTE— Table 2. A summary of MXDFz4.4’s Ly α properties.

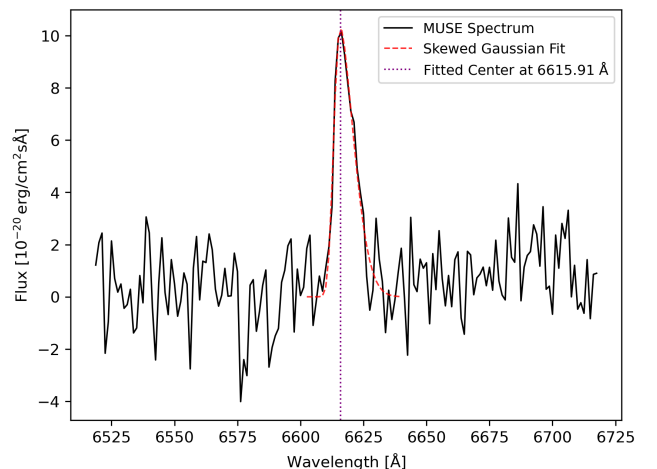


Figure 6. A zoom in on MXDFz4.4’s Ly α emission line. The skewed Gaussian fit to the line, described in §5.1.1, is plotted in red, and the fitted peak of the line at 6615.91 Å is plotted in purple. The properties of the line derived from the fit are detailed in Table 2.

5.1.1. Ly α emission line properties

The simplest Ly α properties we can study are the flux and the equivalent width (EW). LCEs are expected to have strong Ly α emission, as many of the conditions necessary for LyC photon creation and escape also facilitate Ly α photon creation and escape, for example high-mass stars producing ionizing photons, and low HI-density channels in the ISM and CGM. In order to derive the Ly α flux, we perform a custom skewed-Gaussian fit to

the line, closely following the procedure in (R. Bacon et al. 2023). The skewed Gaussian equation we fit is as follows:

$$F(\lambda) = A \left[1 + \operatorname{erf} \left(\frac{\gamma(\lambda - \lambda_0)}{\sqrt{2}\sigma} \right) \right] \exp \left(-\frac{(\lambda - \lambda_0)^2}{2\sigma^2} \right) \quad (3)$$

where A is the amplitude of the Gaussian, λ_0 is the central wavelength, σ is the standard deviation and γ is the asymmetry parameter; large positive γ in this case leading to a more redward-skewed line. The flux of this line is calculated in the same way as a normal Gaussian function:

$$F_{\text{tot}} = \int_{-\infty}^{\infty} F(\lambda) d\lambda = A\sigma\sqrt{2\pi}. \quad (4)$$

We subtract the background from this flux measured in two representative windows of 66.25 \AA (53 MUSE spectral pixels) around the emission line. We subtract the median pixel flux in these two windows multiplied by the number of pixels underneath the Ly α line. The final Ly α flux is $93 \pm 8 \times 10^{-20} \text{ erg/s/cm}^2$. This is completely consistent with the value from the public MXDF catalog (R. Bacon et al. 2023). As there is no continuum detected in the MUSE data, we then calculate the Ly α EW by taking the ratio of the Ly α flux to the flux in the filter that sees the 1216 \AA emission, F606W, having first subtracted the Ly α flux from this filter. The result is an observed Ly α EW of $95 \pm 11 \text{ \AA}$ which gives a rest frame EW of $17 \pm 2 \text{ \AA}$.

We compare this Ly α EW with literature results in Fig. 7, where we shade in red the full region that MXDFz4.4 could occupy in terms of f_{esc} , and $\pm 1\sigma$ in terms of Ly α EW. This region is outside the range of results from low-redshift (S. R. Flury et al. 2022b), although there is significant scatter (grey points). However, this region is also in significant disagreement with the relation at high-redshift established by A. J. Pahl et al. (2021). However, it is expected that at very high f_{esc} , the Ly α EW would not be a good tracer. This stems from the necessary reduction in nebular emission when a high fraction of ionizing photons escape the galaxy, rather than powering the nebular emission from the ISM.

The situation is slightly different for the Ly α escape fraction, $f_{\text{esc,Ly}\alpha}$. If the $f_{\text{esc,Ly}\alpha}$ is calculated using non-resonant hydrogen lines, such as H α , it should scale with f_{esc} even to high f_{esc} values. A close relation between f_{esc} and $f_{\text{esc,Ly}\alpha}$ has indeed been found (S. R. Flury et al. 2022b; A. E. Jaskot et al. 2024; A. E. Jaskot 2025). However, as we do not have access to these lines for MXDFz4.4, we resort to comparing f_{esc} to $f_{\text{esc,Ly}\alpha}$ calculated using our SED fitting, and the UV magnitude in the F775W filter.

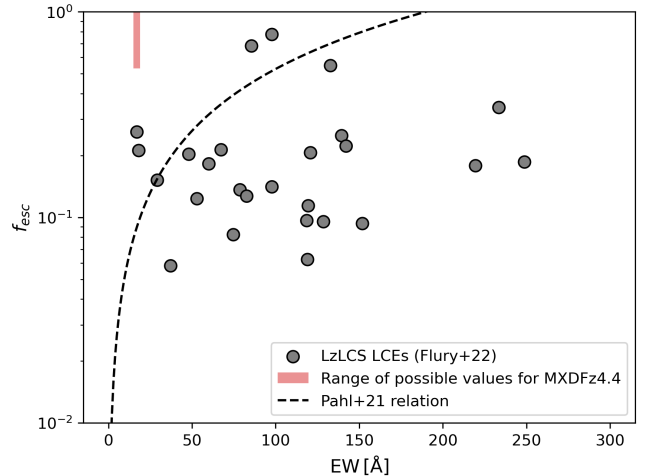


Figure 7. Ly α EW vs f_{esc} , with the range of possible values for MXDFz4.4 highlighted in light red. The darker red area denotes the range derived using the $L_{1500}/L_{\text{Ly}\alpha}$ value from CIGALE. The literature results (grey points) are collected by S. R. Flury et al. (2022b) (low- z) and the dashed relation is from A. J. Pahl et al. (2021) (high- z). The red area representing MXDFz4.4 has a width of $\pm 1\sigma$ in Ly α EW and the full range of possible values for f_{esc} : 27 – 100%.

We calculate the $f_{\text{esc,Ly}\alpha}$ using the dust-corrected SFRs from our CIGALE runs. As our SED fitting suggests the SFR has evolved dramatically over the last 100 Myr, and even likely over the last 10 Myr we consider both averaged SFR values (see Table 1). In the past, Ly α escape has been calculated using both UV-derived SFRs and H α -derived SFRs; our results for the 100 Myr-averaged SFRs can be more readily compared with the UV-based method, and 10 Myr results with the H α method. We therefore give a range of possible $f_{\text{esc,Ly}\alpha}$ values in Table 2 (individual uncertainties are far smaller than the range), for the BC03 models, the BPASS models and also a comparison to the value derived using the UV magnitude simply converted to an SFR following the standard prescription from R. C. Kennicutt (1998). We caution that this prescription assumes a constant SFR over more than 100 Myr, which is very unlikely to be the case for MXDFz4.4. The Ly α escape fractions derived are: 8 – 38% (BC03), 27 – 300% (BPASS) and $13 \pm 2\%$ (UV magnitude). Because of the numerous assumptions and model dependencies used to arrive at these values, it is challenging to interpret them in a physically meaningful sense alongside low-redshift results. They vary from quite low, given that MXDFz4.4 is a strong LCE, to as high as expected. Observations of the H α line would be necessary to more reliably determine the MXDFz4.4’s SFR and therefore $f_{\text{esc,Ly}\alpha}$. However, if it is indeed the case that MXDFz4.4 is a very strong LCE, observing its accordingly reduced H α emission may be challenging.

The asymmetry of the Ly α line is generally thought of as resulting from kinematics in the neutral gas in the ISM and CGM, such as outflows, as well as back-scattering. K. Kakiichi & M. Gronke (2021) suggest that galaxies with their ISM in the density-bounded scenario (in which ionizing photons escape) have a lower red peak asymmetry (a more symmetric line). Thus this quantity may provide a simple way to assess the porosity of the ISM, crucial to allowing LyC escape. This is tentatively borne out in the observational sample of Y. I. Izotov et al. (2016, 2018b,a). We define the red peak asymmetry, A_f , similarly to K. Kakiichi & M. Gronke (2021);

$$A_f = \frac{\int_{\lambda_{red\ peak}}^{\infty} f_{\lambda} d\lambda}{\int_{\lambda_{valley}}^{\lambda_{red\ peak}} f_{\lambda} d\lambda}, \quad (5)$$

where f_{λ} is the Ly α flux, $\lambda_{red\ peak}$ is the wavelength at the red peak and λ_{valley} is the wavelength between the red and blue peaks. In this case there is no blue peak, so we take a wavelength 20Å bluewards of the red peak. The resulting A_f is robust to this choice of lower integration limit. We calculate A_f to be 2.1 ± 0.6 , with an uncertainty calculated by MC sampling Eq. 5 within the 1σ limits of our skewed Gaussian fit to the Ly α line. This is a low red peak asymmetry according to K. Kakiichi & M. Gronke (2021), consistent with the galaxies they find to be strong LCEs, with mostly density-bounded ISM conditions.

The FWHM of the Ly α line is, however, in light contradiction with expectations. A. Verhamme et al. (2015) showed that LAEs with narrow peaks, close to the systemic redshift, are good candidates to be LCEs, however MXDFz4.4 has a relatively large FWHM: 405 ± 52 km/s (corrected for the MUSE line spread function). Larger FWHM values generally indicate higher neutral hydrogen column densities, however J. Kerutt et al. (2024) also find reasonably high FWHM values for 12 LCE candidates at $z > 3$, some consistent with MXDFz4.4.

These slightly conflicting results for the spectral properties of MXDFz4.4’s Ly α emission stress the need to also take into account its spatial properties. We do so in the following sections.

5.1.2. Ly α halo fraction

The Ly α halo fraction, HF, is currently the most promising tracer of f_{esc} at low redshift (J. Puschig et al. 2017; A. Saldana-Lopez et al. 2025). Broadly, it encapsulates the amount of Ly α emission that escapes the host galaxy in an extended halo, rather than co-spatially with the UV emission. A low halo fraction indicates the presence of clear channels in the ISM and CGM of the galaxy, through which Ly α

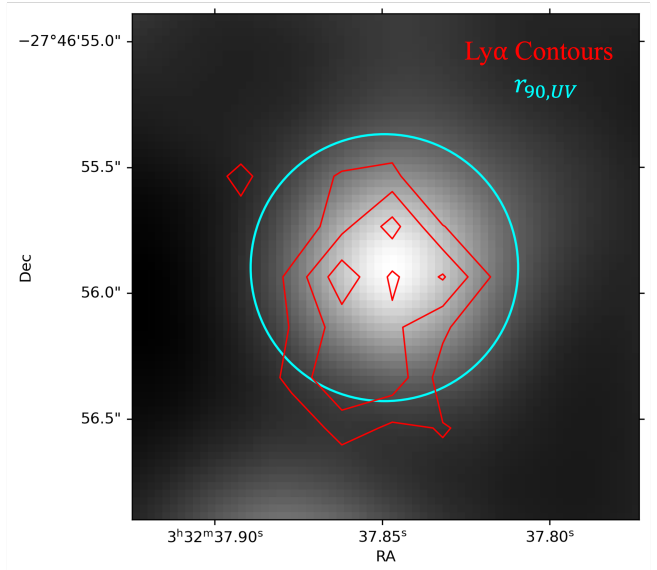


Figure 8. 2, 3, 4 and 5 σ contours of Ly α (red) shown over the F775W image which sees the rest frame UV emission, PSF matched to MUSE. The cyan circle denotes $r_{90,UV}$.

photons escape with minimal scattering events and which facilitate LyC photon escape. A. Saldana-Lopez et al. (2025) fit a relation between the HF and f_{esc} : $\log_{10}(f_{esc}) = (-2.32 \pm 0.41) \times \text{HF} - (0.38 \pm 0.25)$, at low redshift from the Lyman Alpha and Continuum Origins Survey (LaCOS, A. Le Reste et al. 2025). We study this quantity, and its relation to f_{esc} , for the first time at high redshift.

In order to compute the HF for our data, where the Ly α comes from MUSE and the UV continuum comes from HST’s F775W filter, we broadly follow the method laid out by L. Wisotzki et al. (2016) and close to that employed by A. Saldana-Lopez et al. (2025) to facilitate comparison. The key difference between our available data and that of A. Saldana-Lopez et al. (2025) is that Ly α is detected in MUSE rather than HST, and that no continuum is detected in Ly α , so we must combine the two data to calculate the HF.

The MUSE data, is, firstly, a datacube, and a narrow band (NB) image must be created around MXDFz4.4. We create the NB image for our HF calculation by summing the datacube in a 20 Å window around the wavelength of the Ly α emission, which contains all the Ly α flux. However, this NB image still has a much larger PSF than the HST image, so morphological comparisons are not yet possible. We therefore convolve the HST image to the MUSE PSF, using the Moffat profile described in R. Bacon et al. (2023) for the MXDF.

We then cut out a $3 \times 3''$ window around MXDFz4.4 and subtract the local background from each, masking MXDFz4.4 and nearby sources in the process. Nearby

sources remain masked and radial profiles are calculated for both Ly α and UV. These radial profiles are then compared after normalizing the profile to the core of the Ly α profile. The extended Ly α emission over the UV profile is then considered the Ly α halo and the fraction of the total emission that this constitutes is the HF.

Using this method we derive a HF of $0.27_{-0.18}^{+0.15}$. The significant uncertainty on this value stems from the uncertainty on the Ly α profile. As the integrated SNR of the Ly α emission is only $\simeq 11\sigma$, the outskirts of the profile have low SNR. Another issue affects the center of the profile, caused by the size of the MUSE pixels, $0.2''$. In the inner few tenths of arcseconds of the Ly α profile, only a small number of pixels are considered, which raises the uncertainty. Both of these effects naturally stem from the MUSE data, and cannot be mitigated save in a source with much higher SNR (ideally $\geq 30\sigma$ integrated).

We plot MXDFz4.4’s HF on Fig. 9, together with the results from the LaCOS survey (A. Saldana-Lopez et al. 2025). As before, we plot the $\pm 1\sigma$ area for the HF, and the full range of possible escape fractions. This range overlaps is mostly outside the 1σ uncertainty on the relation established by A. Saldana-Lopez et al. (2025); MXDFz4.4 has a higher fraction of Ly α flux emitted in the halo than expected, or equivalently, a higher f_{esc} than expected based on its HF. We note, however, that the single LCE with a similarly high f_{esc} from that study also lies in the region covered by MXDFz4.4, and the next highest- f_{esc} LCE also lies above the relation. The presence of these two LCEs, together with MXDFz4.4, could suggest a change in the slope of this relation at high f_{esc} . A lack of very high f_{esc} LCEs means it is challenging to test the validity of this relation above $f_{esc} \sim 40\%$ where the HF goes to 0 (i.e. all the Ly α emission is contained within the UV r_{90} area). Previous studies based on MUSE data of LAEs reveal that most, perhaps all LAEs could have at least some halo emission (L. Wisotzki et al. 2016; F. Leclercq et al. 2017) so it could be expected that this relation would flatten towards high f_{esc} values.

In summary, while we find encouraging qualitative agreement between MXDFz4.4 and the prediction from low-redshift, the HF calculation using MUSE data is naturally limited for all but very high SNR LAEs. Increased statistics (most likely coming from $z \sim 3$) will also greatly benefit the assessment of whether the HF is a reliable tracer of LyC escape at high-redshift.

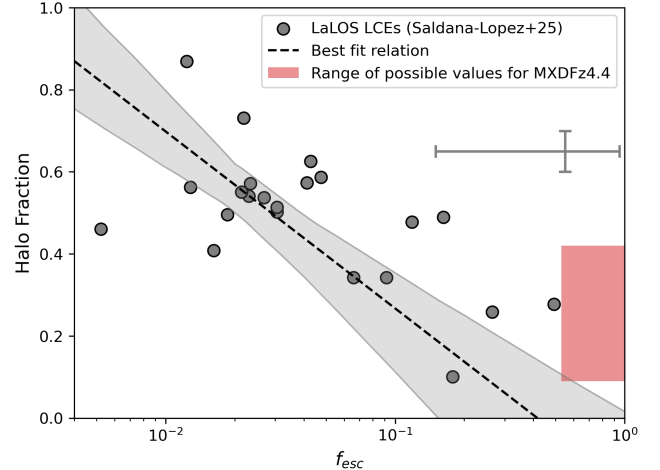


Figure 9. The Ly α Halo Fraction (HF) vs f_{esc} . Grey points, representative error bars, and best-fit relation are from the LaCOS sample in A. Saldana-Lopez et al. (2025). The range of possible values for MXDFz4.4 is highlighted as in Fig. 7.

5.1.3. Ly α r_{50}

Additional Ly α morphological parameters have been suggested as f_{esc} tracers. The compactness of the Ly α emission can be expressed more simply than the HF, using $r_{50, Ly\alpha}$. This has also been shown to be a potentially valuable tracer of f_{esc} (A. Saldana-Lopez et al. 2025), and one which does not rely on a detection of the continuum. More compact galaxies, therefore with lower $r_{50, Ly\alpha}$, exhibit higher f_{esc} values. The suggested interpretation broadly follows the logic used to explain the correlation between the concentration of the UV starlight and f_{esc} (see the following Section). Additionally, as with the interpretation of the HF, Ly α escaping mostly centrally indicates clear channels through the ISM towards the observer, which also elevate f_{esc} .

We derive $r_{50, Ly\alpha}$ for MXDFz4.4, via forward modeling of the same local background-subtracted NB image as for the HF. The intrinsic surface brightness distribution is modeled as a Sersic profile and convolved with the MUSE PSF (see §2). Parameters are inferred using MCMC sampling with the python package emcee (D. Foreman-Mackey et al. 2013, 2019).

We find a MUSE PSF-adjusted $r_{50, Ly\alpha}$ value of $2.4_{-0.5}^{+0.6}$ kpc, which we plot as the red shaded area in Fig. 10 together with the results from A. Saldana-Lopez et al. (2025), where once again this area encompasses the full range of possible f_{esc} values and $\pm 1\sigma$ in $r_{50, Ly\alpha}$. We find less agreement here than in the HF, with the region demarcating MXDFz4.4 significantly outside the grey uncertainty region from A. Saldana-Lopez et al. (2025). However, we note that there are other LAEs of high f_{esc} that reside above this region, showing more

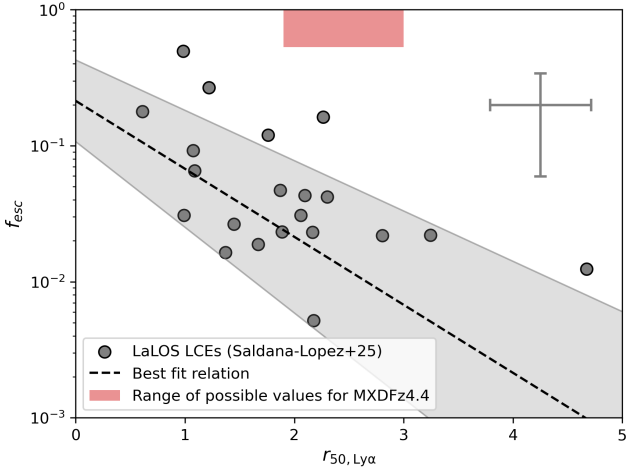


Figure 10. MXDFz4.4’s $r_{50, Ly\alpha}$, plotted against its f_{esc} , compared to the sample of A. Saldana-Lopez et al. (2025) in grey. Colours denote the same as in Figs. 7 and 9.

extended Ly α emission than would be expected given their escape fractions.

Following a similar logic to $r_{50, Ly\alpha}$, the offset of the Ly α and UV centroids has also been suggested as a tracer of f_{esc} (A. Saldana-Lopez et al. 2025) through the $\frac{\Delta_{Ly\alpha-UV}}{r_{90, UV}}$ statistic. However, the value we measure is consistent with 0 after accounting for uncertainties introduced by a potential, small WCS offset between F775W and MUSE, of the order expected when comparing images of extremely different pixel sizes (10-20% of the larger pixel size, in this case $0''.02 - 0''.04$), as well as the centroiding uncertainty itself, particularly for MXDFz4.4’s clearly non-Gaussian profile. We therefore accept that it will always be challenging to extract significant conclusions from this statistic when using the combination of MUSE and HST/JWST data.

5.2. Star formation rate surface density, Σ_{SFR}

A high SFR surface density, Σ_{SFR} , has been highlighted as a galaxy property which can correlate with f_{esc} (Y. I. Izotov et al. 2016; R. P. Naidu et al. 2020; S. Gazagnes et al. 2020; A. E. Jaskot et al. 2024). The explanation centers on stellar feedback which can create holes in the ISM, and does so more efficiently when the stellar environment is more concentrated (higher Σ_{SFR}).

We define Σ_{SFR} within MXDFz4.4’s UV half-light radius, using the typical equation for Σ_{SFR} (T. Shibuya et al. 2019; R. P. Naidu et al. 2020): $\Sigma_{SFR} = \frac{SFR/2}{\pi r_{50}^2}$. MXDFz4.4’s $r_{50} = 0.63 \pm 0.04$ kpc. This half-light radius is derived in K. V. Nedkova et al. (2024) using a multi-wavelength version of GALFIT (C. Y. Peng et al. 2002, 2010) that fits Sérsic profiles in all available filters simultaneously (B. Häußler et al. 2013). For MXDFz4.4,

30 mas CANDELS imaging (A. M. Koekemoer et al. 2011) in nine filters are used to constrain the half-light radius: F435W, F606W, F775W, F814W, F850LP, F105W, F125W, F140W, and F160W. While the re-processing of the ACS/WFC imaging as part of the HST archival program ID 16621 provide significant improvements to the image quality, these improvements are most significant in F435W, and less so in F775W, from which we measure the half-light radius. We therefore opt to use the results from K. V. Nedkova et al. (2024) that are constrained over multiple wavelengths, noting that we also find good agreement using the `photutils` package on the re-processed F775W image, lending confidence to this result.

We derive a number of different SFRs for MXDFz4.4 (see Table 1) based on SED fitting and different timescales (10 – 100 Myr). The low end of these ranges gives Σ_{SFR} values less than $1 M_{\odot}/\text{yr}/\text{kpc}^2$, which appears far too low for a strong LCE such as MXDFz4.4. The higher end of these ranges ($\gtrsim 10 M_{\odot}/\text{yr}$) gives moderate Σ_{SFR} values around $5 - 6 M_{\odot}/\text{yr}/\text{kpc}^2$. This is still not high considering the very high f_{esc} MXDFz4.4 likely exhibits. However, when looking in more detail at the SFH plots produced by CIGALE, the peaks of the recent burst (which is present in the SFH regardless of stellar population model choice) are around $9 M_{\odot}/\text{yr}$ (BPASS) and $40 M_{\odot}/\text{yr}$ (BC03). $40 M_{\odot}/\text{yr}$ gives a Σ_{SFR} value of $17 M_{\odot}/\text{yr}/\text{kpc}^2$, which is more as expected for a strong LCE (A. E. Jaskot et al. 2024). However, peak SFRs such as these are not typically used for this calculation. The fact that MXDFz4.4 only has a Σ_{SFR} in line with low-redshift predictions when the peak of the recent starburst is considered is likely further evidence of the impact of this burst on the escape of LyC photons.

Although there is less of a correlation found between f_{esc} and sSFR (specific star-formation rate; SFR divided by stellar mass), we note that most of the strong LzLCS LCEs have sSFR values above $10^{-8} (\text{yr}^{-1})$, between $10^{-8} (\text{yr}^{-1})$ and $10^{-7} (\text{yr}^{-1})$ (S. R. Flury et al. 2022b). High f_{esc} in high sSFR galaxies is also found in simulations (S. H. Menon et al. 2025). Using the same SFR ranges, and our CIGALE +BPASS-derived stellar mass of $10^{8.3} M_{\odot}$, we derive sSFR values between $1.2 \times 10^{-8} (\text{yr}^{-1})$ and $6 \times 10^{-8} (\text{yr}^{-1})$, consistent with the LCEs of very high f_{esc} in S. R. Flury et al. (2022b).

5.3. UV slope

The UV slope, β , has been suggested as a promising tracer of f_{esc} at low redshift (J. Chisholm et al. 2022). It is particularly attractive as it is easy to measure at any redshift (albeit subject to uncertainties, e.g. D. Austin et al. 2025). The UV slope is sensitive to the dust con-

tent of the galaxy as dust absorbs these UV photons and re-emits them in the infrared. The UV slope is additionally sensitive to the age and metallicity of the stellar population, with younger, metal-poor populations having bluer (more negative) slopes. However, nebular continuum - emission from hot gas in the ISM - created by such populations, serves to redden the UV slope. It is argued that the main sensitivity of β is dust, and that as such, a bluer slope - less dust - should correlate with higher escape fractions of LyC photons. This is indeed found at low redshift (J. Chisholm et al. 2022).

We fit the UV slope of MXDFz4.4 and find a redder slope than expected based on the relation found by J. Chisholm et al. (2022), both in the best-fit spectra from CIGALE and in the photometry. Avoiding the 2175 Å feature in the spectrum by calculating the slope in windows of 1250–1750 Å and 2400–2600 Å, we obtain values using CIGALE and BC03 similar to that derived using the observed photometry: $\beta = -1.4_{-0.4}^{+0.3}$. J. Chisholm et al. (2022) find that galaxies with very high f_{esc} , such as MXDFz4.4 ($f_{esc} \gtrsim 20\%$), mostly have $\beta < -2.6$. This suggests the presence of greater dust content than would be expected for a strong LCE, although the older, more chemically evolved component of the composite stellar population found by our SED fitting could also play a role in reddening the UV slope. We note that using the best-fit spectrum from CIGALE and BPASS gives a bluer slope, but that these fits fit the observed photometry slightly less well in the wavelength range where the UV slope is calculated (Fig. 3).

We also caution that while the UV slope does depend on the dust attenuation along the line of sight - the same line of sight as the escape of LyC photons - it is far less impacted by morphology and the potential presence of clear channels in the ISM. The same goes for the escape of Ly α , recently highlighted by V. Markov et al. (2025); T. Ejdetjärn et al. (2026); different components of galaxies can contain differing amounts of dust and neutral hydrogen in their ISM, allowing LyC escape from some but not other parts of the galaxy. Hence the integrated light of a galaxy may show the presence of some dust, despite the existence of dust-clear channels through which LyC escapes (Z. Ji et al. 2025).

6. DISCUSSION

In this section we collect the measured properties of MXDFz4.4, as well as those that are dependent on models, and discuss the validity of those models and the likely nature of MXDFz4.4.

Due to its very high redshift, and therefore the high opacity of the IGM, even in more transmissive sightlines, we conclude that MXDFz4.4’s intrinsic escape fraction

is very high, likely $\geq 50\%$. Given that an escape fraction of $> 100\%$ is unphysical, we are left with two avenues to explain the detection of MXDFz4.4, based on Eq. 1. Either the intrinsic luminosity ratio of non-ionizing to ionizing photons (the second term) must be low, or the transmission of the IGM must be low (the third term).

We consider the two cases from Table 1; using L_{1500}/L_{LyC} from stellar models (pySTARBURST and BPASS) and using L_{1500}/L_{LyC} directly from CIGALE (which includes dust). In the first case, for the dust attenuations we derive with CIGALE, L_{1500}/L_{LyC} must be ≤ 1.88 ($A_v = 0.68$) or ≤ 1.38 ($A_v = 0.34$). In either case L_{1500}/L_{LyC} must be close to unity. This brings MXDFz4.4’s observed f_{esc} into consistency with models of IGM transmission. For the CIGALE-derived case L_{1500}/L_{LyC} must also be very near unity to avoid $f_{esc,abs}^{IGM} > 100\%$. As we can see from Fig. 4, L_{1500}/L_{LyC} ratios of near unity are achieved only by very young and/or very metal-poor populations.

Even with such extreme stellar populations, only a small fraction of sightlines are transmissive enough, according to our modeling (§3.2 and Fig. 5), to allow the f_{esc} that we observe from MXDFz4.4. Using the stellar modelling approach (row 2 of Table 1), a T_{IGM} value of > 10.4 is necessary to ensure $f_{esc,abs}^{IGM} < 100\%$ even with the best case dust attenuation. This is satisfied by just over 2% of sightlines. Using the CIGALE approach (rows 3 and 4 of Table 1), this reduces to 0.3% of sightlines ($T_{IGM} < 0.18$). This can be interpreted as a “ 3σ -unlikely sightline”. The previous case, $T_{IGM} > 10.4$, is equivalent to a little over 2σ unlikely.

It is possible that the IGM actually allows a greater transmission of ionizing photons than the TAOIST models predict. Although the HI CDDF used by TAOIST is redshift dependent, it is primarily calibrated using observations from the Keck Baryonic Structure Survey (KBSS, G. C. Rudie et al. 2013) at $2 \lesssim z \lesssim 3$, and may therefore be inaccurate close to the EoR. TAOIST and other Monte-Carlo based IGM codes also generally do not account for HI clustering, which can be due to large scale structure (C. M. Scarlata et al. 2025). This could also increase the transmission of the most transparent sightlines and reduce the possible tension (K. Kakiichi et al. 2018).

Given, however, that we do observe ionizing escape from MXDFz4.4, and that a young and/or potentially very metal poor stellar population can account for this, we now discuss its physical nature, combining all the f_{esc} tracers we have analyzed and physical conditions we have derived. We caution that comparisons to other LCE samples may be limited by the lack of many LCEs of very high f_{esc} in the literature.

The Ly α EW is in significant disagreement both with results found at low redshift and at high redshift (S. R. Flury et al. 2022b; A. J. Pahl et al. 2021). However, this may be expected for an LCE of very high f_{esc} , as MXDFz4.4 is likely to be. The strength of nebular lines is expected to reduce if significant amounts of ionizing photons escape, as these then no longer go to producing recombination lines like Ly α .

For this reason, $f_{esc, Ly\alpha}$ is expected to correlate with f_{esc} up to very high values, however only if it is calculated using non-resonant hydrogen recombination lines, such as H α . This is not the case for MXDFz4.4 and given the difficulty in deriving precise SFRs using SED fitting, we are left with a large range of $f_{esc, Ly\alpha}$ values, derived in a number of ways. High values, as would be expected, are included, but unfortunately our results are not very constraining and therefore are difficult to compare to others in the literature.

Considering the Ly α asymmetry and HF, these agree fairly well in that a low HF indicates a direct path for LyC photons to escape the galaxy towards the observer, and a symmetric line suggests a density-bounded scenario which also allows high levels of escape.

The high FWHM, however, is less in line with expectations from simulations and low redshift, as this can indicate high neutral hydrogen column densities, which would impede LyC escape. These slightly contradictory Ly α properties may be explained by the effect of the recent burst combined with an older, more evolved population (which likely exists given the redder-than-expected UV slope). Ly α photons can take time to escape from the galaxy (e.g. J. M. Mas-Hesse et al. 2003). At stellar ages less than ~ 2.5 Myr, Ly α struggles to escape from the molecular clouds surrounding stars (M. Hayes et al. 2007). Feedback from massive stars, winds, and the first supernovae, such as we expect in MXDFz4.4's recent burst, then progressively clears the clouds and facilitates both Ly α and LyC escape (D. Rahner et al. 2017; M. Trebitsch et al. 2017; C. A. Carr et al. 2025; L. Komarova et al. 2025). If the burst in MXDFz4.4 is at this stage, rapid development of the emergent Ly α emission would be expected, with some component remaining from the older stellar population and its ISM.

If MXDFz4.4's Ly α line is close to the systemic redshift, which has been shown to correlate well with f_{esc} (A. Verhamme et al. 2015, 2017; S. R. Flury et al. 2022b), this may alleviate the unexpectedly high FWHM. It would mean that significant fraction of the Ly α photons are escaping at the systemic redshift, rather than undergoing an extensive radiative transfer process through surrounding neutral hydrogen. This would help to explain the high fraction of LyC photons

that also escape. Unfortunately we lack the additional lines in MXDFz4.4's spectrum to verify this.

Among all the Ly α -based tracers, we note that one of the most promising at low redshift, the HF, qualitatively agrees with predictions, which moderately increases the confidence in the possibility of using it at high redshift. Further confidence would necessitate testing the HF method for much larger samples, especially in the lower escape fraction regime where the HF relation from A. Saldana-Lopez et al. (2025) is more constrained. Samples of LCEs in the f_{esc} range of MXDFz4.4 are likely to remain small for the foreseeable future, although will remain desirable to better constrain the high- f_{esc} regime, and probe the potential turnover in this relation.

With these conclusions based on MXDFz4.4's Ly α properties in mind, we suggest that the MXDFz4.4's recent star formation and the nature of its burst are the driving force behind its high observed escape fraction, and highlight the importance of the UV and star-formation-related properties in tracing this: Σ_{SFR} and sSFR. It may be for this reason that the Ly α HF still acts as a good tracer of f_{esc} , while for example the Ly α r_{50} is less in line with low-redshift findings (A. Saldana-Lopez et al. 2025); the HF is the most sensitive of the Ly α diagnostics to the holes created in the ISM for Ly α and LyC to escape. Still, the Σ_{SFR} is lower than expected for all but the peak of the recent star formation, which likely means that the nature of the stellar population also plays a significant role, i.e. a young, metal-poor stellar population producing many ionizing photons per UV photon. To illustrate the importance of this, we refer the reader to the earlier discussion about the necessity of L_{1500}/L_{LyC} being near unity (note that this keeps all other parameters, as well as the actual escape of LyC photons, the same). Even the upper bounds on the possible L_{1500}/L_{LyC} ratios we calculate are low compared to the average galaxy population, and are surpassed, according to Fig. 4 for all but the most metal poor stars in 6 – 7 Myr.

Therefore it is likely that the very young and potentially metal-poor nature of the stellar population in MXDFz4.4's recent burst is contributing strongly to its observation as an LCE. This is supported by the recent local Universe work of T. Ejdetjärn et al. (2026), where LyC is boosted due to recent star formation, and LyC emission is not necessarily co-spatial with Ly α , which they attribute to different locations of the LyC-emitting stars and the Ly α emission in the ISM. A boost in the f_{esc} of a galaxy post-starburst has been well studied, especially in simulations (N. Y. Gnedin et al. 2008; H. Yajima et al. 2009; T. Kimm & R. Cen 2014; M. Trebitsch et al. 2017; J. Rosdahl et al. 2022; S. H. Menon et al.

2025), but also in observations (S. R. Flury et al. 2025; L. Komarova et al. 2025; C. A. Carr et al. 2025), with these studies also commenting on the importance of young, metal-poor stars in this process.

The burstiness of early galaxies, within the EoR, has recently been invoked to explain the excess of UV-bright galaxies observed at very high redshifts (G. Sun et al. 2023; X. Shen et al. 2023), and these galaxies have already been suggested as efficient ionizers (R. Endsley et al. 2023; C. Simmonds et al. 2024), mostly due to their enhanced ionizing photon production efficiency, but also due to a potential higher f_{esc} (R. Endsley et al. 2024). Our interpretation of MXDFz4.4’s properties supports this, and suggests that galaxies with successive strong bursts of star formation, may also experience episodes of extremely high LyC production and f_{esc} . We caution that this is a function of metallicity, and that more enriched populations would not produce as many ionizing photons, such that successive bursts may produce fewer and fewer. However, elevated Σ_{SFR} and sSFR during the burst may still facilitate high levels of escape. Such bursty galaxies are therefore strong candidates to emit a large share of the ionizing photons needed to reionize the IGM at early times.

If high-redshift galaxies have a duty cycle closer to 1 (i.e. they spend close to 100% of their time in the burst phase), it might provide a mechanism for EoR galaxies to emit enough ionizing photons into the IGM to create the reionization history that we observe, a similar argument to that presented in R. P. Naidu et al. (2020) for Σ_{SFR} . For this reionization history, the necessary escape fraction on a population level has generally been placed around 5% (S. L. Finkelstein et al. 2019), which is far greater than what we observe in the local Universe. The increased burstiness of high redshift galaxies might therefore help alleviate this issue.

7. SUMMARY AND CONCLUSIONS

We present the detection of the highest-redshift Lyman continuum emitter to date, MXDFz4.4, at $z = 4.442$. This redshift is confirmed by a high-confidence Ly α line in extremely deep, 140h MUSE spectroscopy. MXDFz4.4 has LyC flux measurement in HST’s F435W filter of 8.0σ . We apply all available tracers established by studies at low redshift and conclude the following about the nature of MXDFz4.4:

- Our SED fitting with CIGALE and two different stellar population models, BC03 (G. Bruzual & S. Charlot 2003) and BPASS (J. J. Eldridge et al. 2017) (Fig. 3), suggests a very recent and vigorous burst of star formation, with numerous stellar models predicting a very low L_{1500}/L_{LyC} ra-

tio at these young ages. This would mean that MXDFz4.4’s observed escape fraction is not in tension with models of IGM transmission at $z = 4.44$.

- MXDFz4.4’s Ly α EW is low (Fig. 7), when compared to both low and high-redshift results from the literature. However this may be explained by MXDFz4.4’s very high escape fraction. When f_{esc} is very high, nebular emission, including Ly α , is expected to decrease as ionizing photons are escaping rather than being absorbed and re-emitted as Ly α .
- MXDFz4.4’s Ly α escape fraction, $f_{esc,Ly\alpha}$, is challenging to constrain without the H α emission line. We use SED fitting instead, and MXDFz4.4’s UV magnitude, and find a wide range of $f_{esc,Ly\alpha}$ values, ranging from low to 100%.
- The Ly α FWHM and asymmetry are in slight conflict, with the symmetric line as expected for a strong LCE, but the FWHM of the line higher than expected given expectations from simulations. This may be alleviated by MXDFz4.4’s Ly α line being close to the systemic redshift, shown to be important in facilitating LyC escape, however we lack the other emission lines to assess this.
- The Ly α half-light radius, $r_{50,Ly\alpha}$, is also larger than expected for high- f_{esc} galaxies, outside of the predicted range based on low-redshift results. Both this and the Ly α line FWHM could be attributed to a rapid evolution of the MXDFz4.4’s Ly α emission due to its recent burst, and some contribution from an older stellar population, as well as more chemically evolved parts of the galaxy.
- We tested the promising halo fraction tracer established by A. Saldana-Lopez et al. (2025) for the first time at high redshift and find qualitative agreement with low-redshift results, although MXDFz4.4 occupies a sparsely populated area of the parameter space. Nevertheless, our results support the use of this promising tracer for high-redshift f_{esc} studies. This reinforces the importance of geometry and orientation/viewing angle in the observation of escaping LyC photons. However, we caution that a higher f_{esc} uncertainty may be necessary when deriving f_{esc} using the HF at low HF values, due to a potential flattening of the relation at low HF. More high- f_{esc} LAEs are needed to confirm.

- Among MXDFz4.4’s star formation properties, sSFR is elevated, and Σ_{SFR} is moderate, rising to very elevated when we consider the peak SFR of the recent burst. Both of these point to the importance of the recent burst of star formation in clearing the ISM and facilitating LyC escape.
- We find a higher UV slope, β , than expected, ~ -1.4 both from photometry and the best-fit CIGALE model. This indicates the presence of some dust in the galaxy and means it is likely we are observing the LyC escaping thanks to a specific ISM geometry, also likely due to feedback from the recent burst.

We suggest, based on these results that galaxies in the early Universe, which have been shown to undergo multiple bursts of vigorous star formation, may also undergo successive periods of extremely high ionizing photon production and escape, although the production is likely also dependent on metallicity. While more work is needed to confirm this, the bursty nature of high-redshift galaxies may provide an explanation for the discrepancy between the low levels of f_{esc} observed among the general galaxy population at low redshift and the number needed to reionize the IGM.

While the detection and characterization of MXDFz4.4 shows MUSE to be an extremely useful in-

strument for high-redshift LCE investigation, we warn that the HF method will not work with all MUSE-detected LAEs, as a significant fraction (10-30%, depending on the relative depths of the MUSE data and photometry) are undetected in the continuum (R. Bacon et al. 2023; I. Goovaerts et al. 2023). The $r_{50, Ly\alpha}$ however, accompanied by all the line shape diagnostics, would remain available, making MUSE an efficient instrument to quantify f_{esc} in LAEs up to $z \sim 6.5$, well into the end of the EoR.

ACKNOWLEDGMENTS

Based on observations with the NASA/ESA Hubble Space Telescope obtained at the Space Telescope Science Institute, which is operated by the Association of Universities for Research in Astronomy, Incorporated, under NASA contract NAS5-26555. Support for Program number 16621 provided through a grant from the STScI under NASA contract NAS5-26555. MJH is supported by the Swedish Research Council (Vetenskapsrådet) and is Fellow of the Knut & Alice Wallenberg Foundation.

Facilities:

Software:

APPENDIX

A. REDSHIFT CONFIDENCE

In order to confirm the redshift of MXDFz4.4, we carried out a number of tests, positing the alternative possibilities that the emission line seen in the MUSE spectrum at 6615.9 Å is not Ly α but instead the [O II] λ 3727 doublet, the stronger of the two [O III] lines (5007 Å), H α and the C III] doublet. The first three cases are shown below in the cutouts in Fig. 11, clearly showing the lack of the other expected lines in the spectra. In the case of [O II] and C III], we show plots of [O II] and C III] emitters from the MUSE database in Figs. 12 and 13, clearly showing that both of these doublets are resolved at the wavelength that we observe Ly α in MXDFz4.4. It is therefore clear that none of these cases are plausible.

In the case of H α , we do not see either [O III], [N II] or S II. Additionally, the line at 6615.9 Å is visibly skewed, common for Ly α but extremely uncommon for H α . Finally, if this line was H α , the redshift would be $z = 0.008$, and detections would be expected even in the shallower F336W, F275W and F225W images (Fig. 1) depending on the SED shape, all of which contain non-detections. Finally, the source’s compact morphology is not consistent with a galaxy at $z = 0.008$.

If the line were to be the [O II] λ 3727 doublet, we would expect it to be resolved at the spectral resolution of MUSE. We show the spectrum of an [O II] emitter at the same SNR ($\sim 11\sigma$) and wavelength and show that it is easily resolved (Fig. 12). Additionally, neither [O III] nor H β is detected. Even in the case of a very low ionization state, where [O II] is expected to be stronger than [O III], for an 11σ [O II] detection, we would expect a $> 4\sigma$ detection of the stronger [O III] line (based on an [O III]/[O II] ratio of 0.5, typically found in metal-rich low- z galaxies).

If the line at 6615.9 Å were to be the stronger of the two [O III] lines, we would expect to detect the weaker line at $3 - 4\sigma$ as this line ratio is ~ 3 (independent of astrophysical conditions in the galaxy). In addition to this, not one of H α , H β or [O II] is detected.

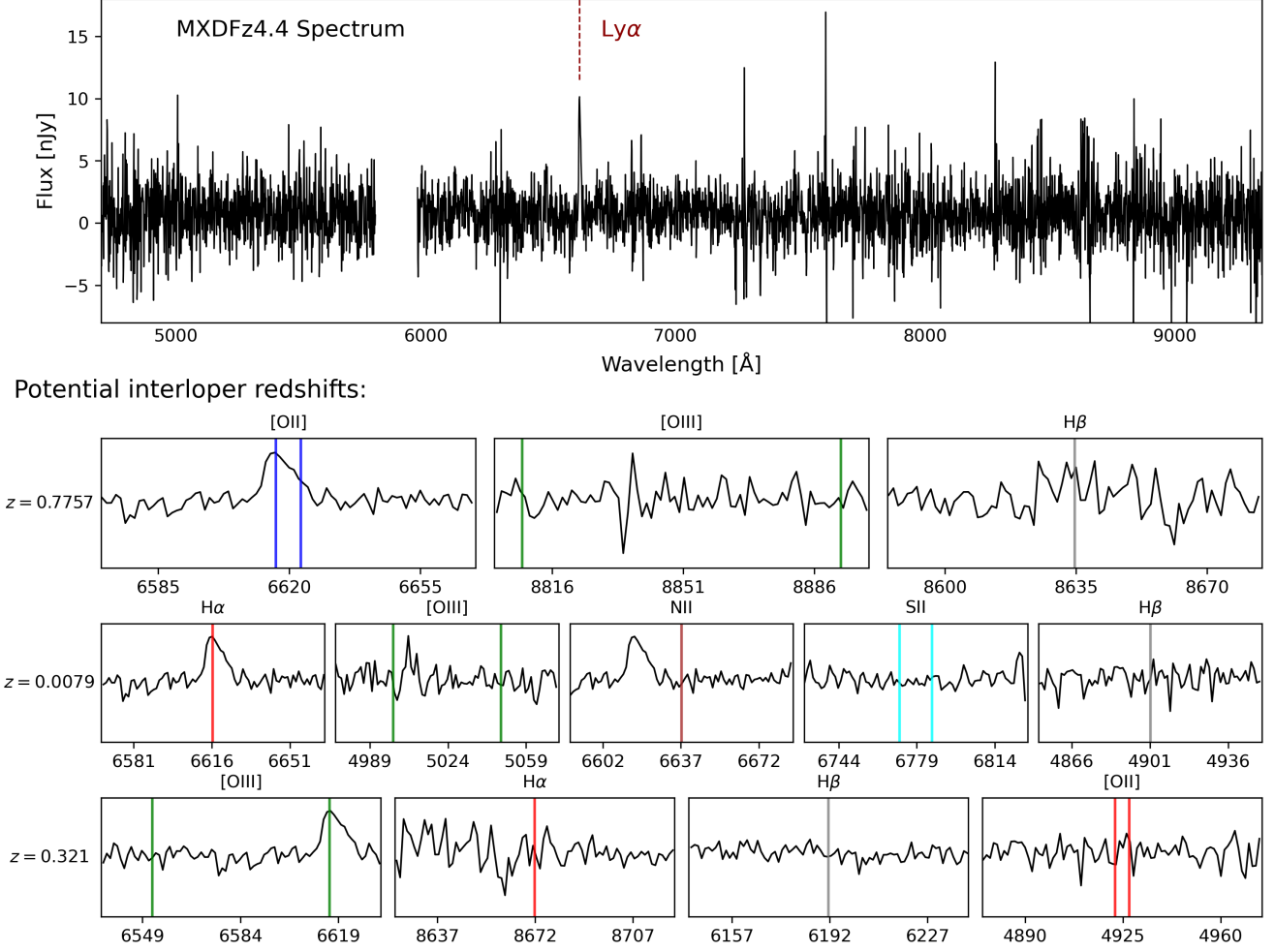


Figure 11. Testing potential interlopers for MXDFz4.4. We posit that the line at 6615.9 Å could be [O II], [O III] and H α , and check for other lines at the corresponding redshifts. The top spectrum is the full MUSE spectrum of MXDFz4.4, each row of cutouts below represents a different interloper redshift, noted on the left. The first row plots the case of [O II] ($z = 0.7757$) and clearly shows the lack of [O III] or H β . The second row plots the case of H α , where we see that [O III] and H β are not detected. The third row plots the case of [O III], where we show the blue [O III] peak is not detected, nor H α , H β , [O II]. These non-detections, combined with the clear asymmetry in the line at 6615.9 Å results in a high redshift confidence for MXDFz4.4.

Finally, Fig. 13 clearly shows that the C III] λ 1907, 1909 doublet is resolved at the wavelength that Ly α is detected in MXDFz4.4’s spectrum.

Together with the clearly asymmetric line-profile, these cases show that there is high confidence in MXDFz4.4’s Ly α line and therefore its redshift of $z = 4.442$.

B. JWST/NIRISS SPECTRUM OF MXDFz4.4 FROM THE NGDEEP PROGRAM

There is JWST/NIRISS Wide-Field Slitless spectroscopy available in the MXDF, from the NGDEEP program (M. B. Bagley et al. 2024). There are no lines detected in MXDFz4.4’s spectrum, despite NGDEEP’s long exposure time in F200W of $>31,000$ sec. However, considering the 5σ flux limit of the spectra 1.2×10^{-18} erg/s/cm 2 /Å, it is unsurprising that no lines are detected. The strongest line that falls in NIRISS’ wavelength coverage is [O II] λ 3727, which would fall at $\sim 2.03 \mu\text{m}$. The 5σ limit of the spectrum is $\sim 30\%$ more than the Ly α flux observed by MUSE, therefore it is not surprising that [O II] is not detected. There are even scenarios of Lyman photon escape, the density-bounded case (see, e.g. Fig. 1 of A. E. Jaskot 2025), where [O II] is suppressed, due to a lack of low-ionization gas in the ISM.

REFERENCES

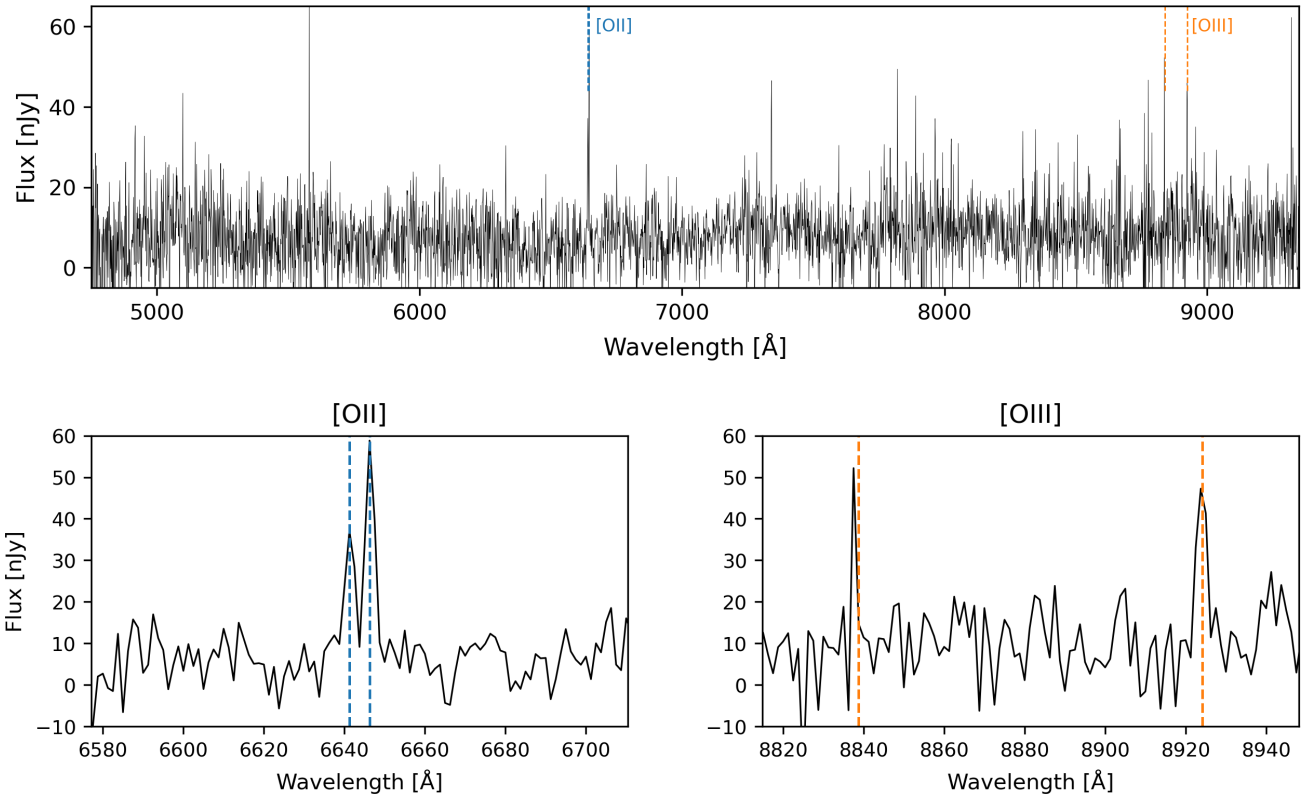


Figure 12. A spectrum of an [O II] emitter at a similar wavelength as MXDFz4.4’s Ly α emission, and with a similar SNR ($\sim 10\sigma$; MUSE object ID: 6969). The double peak is clearly resolved. Additionally, the [O III] doublet is clearly detected, while in MXDFz4.4’s spectrum, only one line is detected.

Asada, Y., Willott, C., Muzzin, A., et al. 2025, arXiv e-prints, arXiv:2507.03124,

doi: [10.48550/arXiv.2507.03124](https://doi.org/10.48550/arXiv.2507.03124)

Austin, D., Conselice, C. J., Adams, N. J., et al. 2025, ApJ, 995, 43, doi: [10.3847/1538-4357/ae07db](https://doi.org/10.3847/1538-4357/ae07db)

Bacon, R., Brinchmann, J., Conseil, S., et al. 2023, A&A, 670, A4, doi: [10.1051/0004-6361/202244187](https://doi.org/10.1051/0004-6361/202244187)

Bagley, M. B., Pirzkal, N., Finkelstein, S. L., et al. 2024, ApJL, 965, L6, doi: [10.3847/2041-8213/ad2f31](https://doi.org/10.3847/2041-8213/ad2f31)

Bassett, R., Ryan-Weber, E. V., Cooke, J., et al. 2021, MNRAS, 502, 108, doi: [10.1093/mnras/stab070](https://doi.org/10.1093/mnras/stab070)

Beckett, A., Rafelski, M., Scarlata, C., et al. 2025, ApJ, 992, 155, doi: [10.3847/1538-4357/ae0291](https://doi.org/10.3847/1538-4357/ae0291)

Beckwith, S. V. W., Stiavelli, M., Koekemoer, A. M., et al. 2006, AJ, 132, 1729, doi: [10.1086/507302](https://doi.org/10.1086/507302)

Bielby, R. M., Fumagalli, M., Fossati, M., et al. 2020, MNRAS, 493, 5336, doi: [10.1093/mnras/staa546](https://doi.org/10.1093/mnras/staa546)

Boquien, M., Burgarella, D., Roehly, Y., et al. 2019, A&A, 622, A103, doi: [10.1051/0004-6361/201834156](https://doi.org/10.1051/0004-6361/201834156)

Bosman, S. E. I., Davies, F. B., Becker, G. D., et al. 2022, MNRAS, 514, 55, doi: [10.1093/mnras/stac1046](https://doi.org/10.1093/mnras/stac1046)

Brammer, G. B., van Dokkum, P. G., Franx, M., et al. 2012, ApJS, 200, 13, doi: [10.1088/0067-0049/200/2/13](https://doi.org/10.1088/0067-0049/200/2/13)

Bruzual, G., & Charlot, S. 2003, MNRAS, 344, 1000, doi: [10.1046/j.1365-8711.2003.06897.x](https://doi.org/10.1046/j.1365-8711.2003.06897.x)

Burgarella, D., Buat, V., & Iglesias-Páramo, J. 2005, MNRAS, 360, 1413, doi: [10.1111/j.1365-2966.2005.09131.x](https://doi.org/10.1111/j.1365-2966.2005.09131.x)

Calzetti, D., Armus, L., Bohlin, R. C., et al. 2000, ApJ, 533, 682, doi: [10.1086/308692](https://doi.org/10.1086/308692)

Carr, C. A., Cen, R., Scarlata, C., et al. 2025, ApJ, 982, 137, doi: [10.3847/1538-4357/adb72f](https://doi.org/10.3847/1538-4357/adb72f)

Chabrier, G. 2003, PASP, 115, 763, doi: [10.1086/376392](https://doi.org/10.1086/376392)

Chisholm, J., Saldana-Lopez, A., Flury, S., et al. 2022, MNRAS, 517, 5104, doi: [10.1093/mnras/stac2874](https://doi.org/10.1093/mnras/stac2874)

Choustikov, N., Katz, H., Saxena, A., et al. 2024, MNRAS, 529, 3751, doi: [10.1093/mnras/stae776](https://doi.org/10.1093/mnras/stae776)

Citro, A., Scarlata, C. M., Mantha, K. B., et al. 2025, ApJ, 986, 184, doi: [10.3847/1538-4357/add5e6](https://doi.org/10.3847/1538-4357/add5e6)

Donnan, C. T., McLure, R. J., Dunlop, J. S., et al. 2024, MNRAS, 533, 3222, doi: [10.1093/mnras/stae2037](https://doi.org/10.1093/mnras/stae2037)

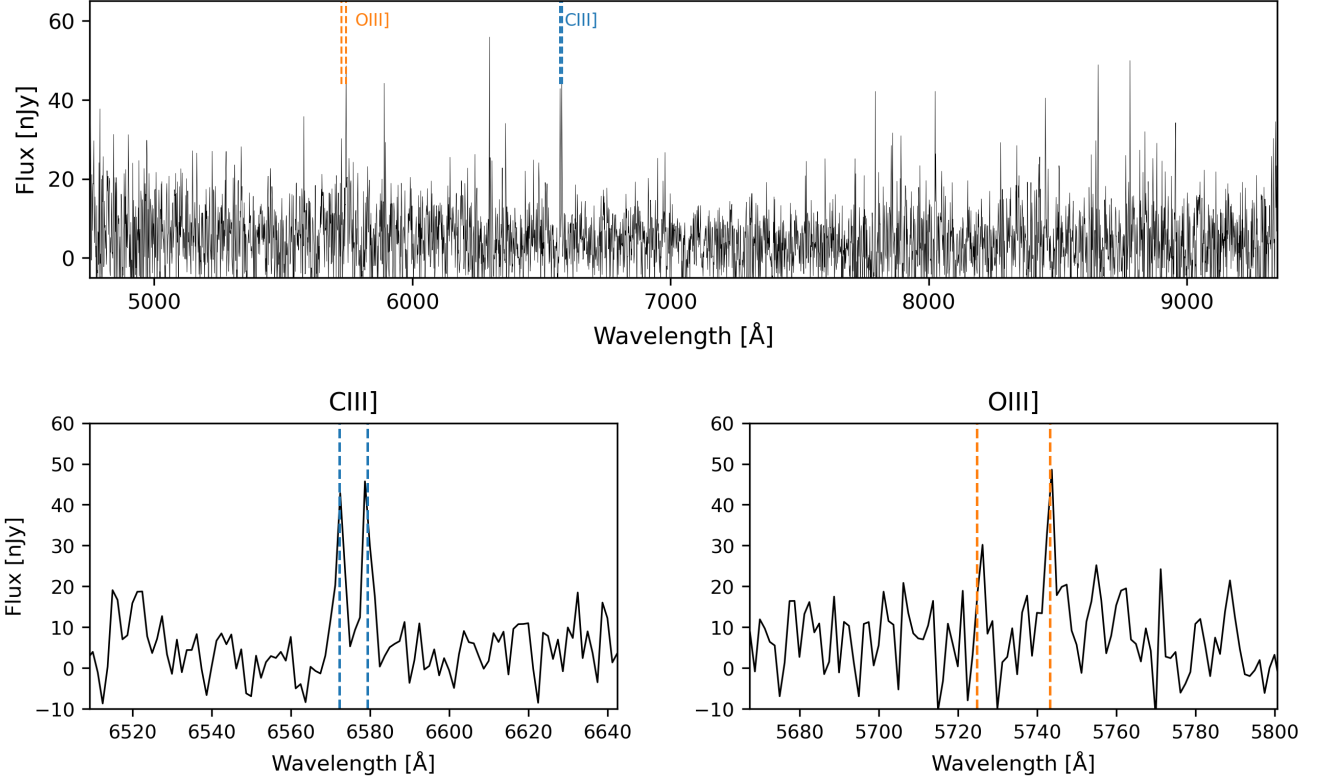


Figure 13. A spectrum of an C III] λ 1907,1909 emitter at a similar wavelength as MXDFz4.4’s Ly α emission, and with a similar SNR ($\sim 7.5\sigma$; MUSE object ID: 1784). The double peak of C III] is clearly resolved. O III] λ 1660,1666 is also clearly detected in the spectrum.

Eisenstein, D. J., Willott, C., Alberts, S., et al. 2023, arXiv e-prints, arXiv:2306.02465,
doi: [10.48550/arXiv.2306.02465](https://doi.org/10.48550/arXiv.2306.02465)

Ejdetjärn, T., Östlin, G., Rosdahl, J., Blaizot, J., & Agertz, O. 2026, arXiv e-prints, arXiv:2601.20943.
<https://arxiv.org/abs/2601.20943>

Eldridge, J. J., Izzard, R. G., & Tout, C. A. 2008, MNRAS, 384, 1109, doi: [10.1111/j.1365-2966.2007.12738.x](https://doi.org/10.1111/j.1365-2966.2007.12738.x)

Eldridge, J. J., Stanway, E. R., Xiao, L., et al. 2017, PASA, 34, e058, doi: [10.1017/pasa.2017.51](https://doi.org/10.1017/pasa.2017.51)

Endsley, R., Stark, D. P., Whitler, L., et al. 2023, MNRAS, 524, 2312, doi: [10.1093/mnras/stad1919](https://doi.org/10.1093/mnras/stad1919)

Endsley, R., Stark, D. P., Whitler, L., et al. 2024, MNRAS, 533, 1111, doi: [10.1093/mnras/stae1857](https://doi.org/10.1093/mnras/stae1857)

Fan, X., Strauss, M. A., Becker, R. H., et al. 2006, AJ, 132, 117, doi: [10.1086/504836](https://doi.org/10.1086/504836)

Finkelstein, S. L., D’Aloisio, A., Paardekooper, J.-P., et al. 2019, ApJ, 879, 36, doi: [10.3847/1538-4357/ab1ea8](https://doi.org/10.3847/1538-4357/ab1ea8)

Finkelstein, S. L., Leung, G. C. K., Bagley, M. B., et al. 2024, ApJL, 969, L2, doi: [10.3847/2041-8213/ad4495](https://doi.org/10.3847/2041-8213/ad4495)

Flury, S. R., Jaskot, A. E., Ferguson, H. C., et al. 2022a, ApJS, 260, 1, doi: [10.3847/1538-4365/ac5331](https://doi.org/10.3847/1538-4365/ac5331)

Flury, S. R., Jaskot, A. E., Ferguson, H. C., et al. 2022b, ApJ, 930, 126, doi: [10.3847/1538-4357/ac61e4](https://doi.org/10.3847/1538-4357/ac61e4)

Flury, S. R., Jaskot, A. E., Saldana-Lopez, A., et al. 2025, ApJ, 985, 128, doi: [10.3847/1538-4357/adc305](https://doi.org/10.3847/1538-4357/adc305)

Foreman-Mackey, D., Hogg, D. W., Lang, D., & Goodman, J. 2013, PASP, 125, 306, doi: [10.1086/670067](https://doi.org/10.1086/670067)

Foreman-Mackey, D., Farr, W., Sinha, M., et al. 2019, The Journal of Open Source Software, 4, 1864, doi: [10.21105/joss.01864](https://doi.org/10.21105/joss.01864)

Gazagnes, S., Chisholm, J., Schaerer, D., Verhamme, A., & Izotov, Y. 2020, A&A, 639, A85, doi: [10.1051/0004-6361/202038096](https://doi.org/10.1051/0004-6361/202038096)

Giavalisco, M., Ferguson, H. C., Koekemoer, A. M., et al. 2004, ApJL, 600, L93, doi: [10.1086/379232](https://doi.org/10.1086/379232)

Gnedin, N. Y., Kravtsov, A. V., & Chen, H.-W. 2008, ApJ, 672, 765, doi: [10.1086/524007](https://doi.org/10.1086/524007)

Goovaerts, I., Pello, R., Thai, T. T., et al. 2023, A&A, 678, A174, doi: [10.1051/0004-6361/202347110](https://doi.org/10.1051/0004-6361/202347110)

Grogin, N. A., Kocevski, D. D., Faber, S. M., et al. 2011, ApJS, 197, 35, doi: [10.1088/0067-0049/197/2/35](https://doi.org/10.1088/0067-0049/197/2/35)

Harikane, Y., Nakajima, K., Ouchi, M., et al. 2024, ApJ, 960, 56, doi: [10.3847/1538-4357/ad0b7e](https://doi.org/10.3847/1538-4357/ad0b7e)

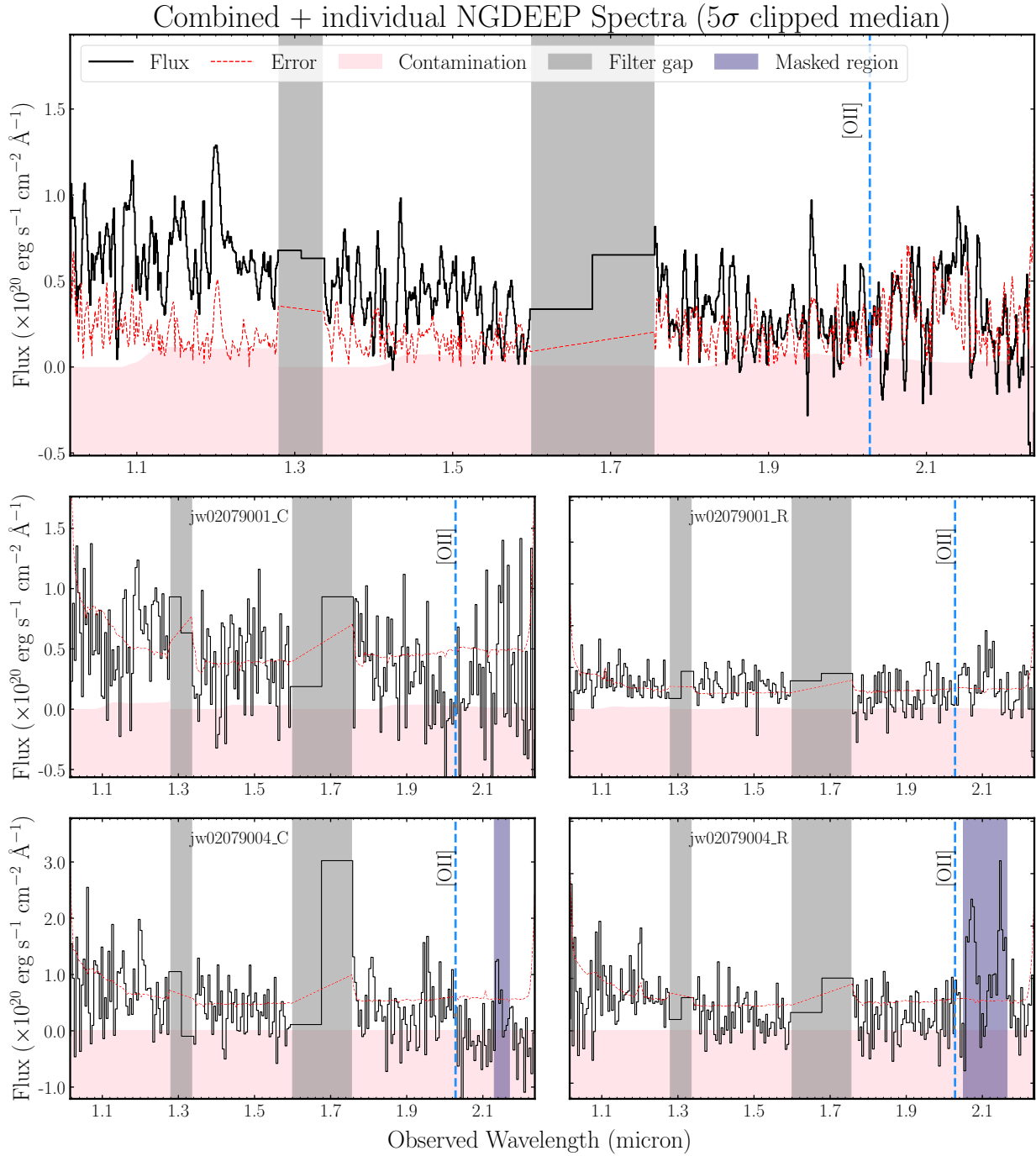


Figure 14. The JWST/NIRISS NGDEEP spectrum of MXDFz4.4 (F115W, F150W and F200W filters). The four individual orientations are shown in the lower panels and the combined (5σ - clipped median) spectrum is shown above. Filter gaps are shaded in grey and contaminants based on the 2D spectra are masked in blue. No lines are detected. The position of [O II] in F200W is shown with a dashed blue line.

- Häußler, B., Bamford, S. P., Vika, M., et al. 2013, *MNRAS*, 430, 330, doi: [10.1093/mnras/sts633](https://doi.org/10.1093/mnras/sts633)
- Hawcroft, C., Leitherer, C., Aranguré, O., et al. 2025, *ApJS*, 280, 5, doi: [10.3847/1538-4365/adddb6](https://doi.org/10.3847/1538-4365/adddb6)
- Hayes, M., Östlin, G., Atek, H., et al. 2007, *MNRAS*, 382, 1465, doi: [10.1111/j.1365-2966.2007.12482.x](https://doi.org/10.1111/j.1365-2966.2007.12482.x)
- Hayes, M. J., Saldana-Lopez, A., Citro, A., et al. 2025, *ApJ*, 982, 14, doi: [10.3847/1538-4357/adaea1](https://doi.org/10.3847/1538-4357/adaea1)
- Henry, A., Scarlata, C., Martin, C. L., & Erb, D. 2015, *ApJ*, 809, 19, doi: [10.1088/0004-637X/809/1/19](https://doi.org/10.1088/0004-637X/809/1/19)
- Horne, K. 1986, *PASP*, 98, 609, doi: [10.1086/131801](https://doi.org/10.1086/131801)
- Hui, L., Stebbins, A., & Burles, S. 1999, *ApJL*, 511, L5, doi: [10.1086/311826](https://doi.org/10.1086/311826)
- Inoue, A. K. 2011, *MNRAS*, 415, 2920, doi: [10.1111/j.1365-2966.2011.18906.x](https://doi.org/10.1111/j.1365-2966.2011.18906.x)
- Inoue, A. K., Shimizu, I., Iwata, I., & Tanaka, M. 2014, *MNRAS*, 442, 1805, doi: [10.1093/mnras/stu936](https://doi.org/10.1093/mnras/stu936)
- Izotov, Y. I., Chisholm, J., Worseck, G., et al. 2022, *MNRAS*, 515, 2864, doi: [10.1093/mnras/stac1899](https://doi.org/10.1093/mnras/stac1899)
- Izotov, Y. I., Schaerer, D., Guseva, N. G., Thuan, T. X., & Worseck, G. 2024a, *MNRAS*, 528, L10, doi: [10.1093/mnras/sladd166](https://doi.org/10.1093/mnras/sladd166)
- Izotov, Y. I., Schaerer, D., Thuan, T. X., et al. 2016, *MNRAS*, 461, 3683, doi: [10.1093/mnras/stw1205](https://doi.org/10.1093/mnras/stw1205)
- Izotov, Y. I., Schaerer, D., Worseck, G., et al. 2018a, *MNRAS*, 474, 4514, doi: [10.1093/mnras/stx3115](https://doi.org/10.1093/mnras/stx3115)
- Izotov, Y. I., Schaerer, D., Worseck, G., et al. 2020, *MNRAS*, 491, 468, doi: [10.1093/mnras/stz3041](https://doi.org/10.1093/mnras/stz3041)
- Izotov, Y. I., Thuan, T. X., Guseva, N. G., et al. 2024b, *MNRAS*, 527, 281, doi: [10.1093/mnras/stad3151](https://doi.org/10.1093/mnras/stad3151)
- Izotov, Y. I., Worseck, G., Schaerer, D., et al. 2018b, *MNRAS*, 478, 4851, doi: [10.1093/mnras/sty1378](https://doi.org/10.1093/mnras/sty1378)
- Jaskot, A. E. 2025, *ARA&A*, 63, 45, doi: [10.1146/annurev-astro-111324-074935](https://doi.org/10.1146/annurev-astro-111324-074935)
- Jaskot, A. E., Silveyra, A. C., Plantinga, A., et al. 2024, *ApJ*, 972, 92, doi: [10.3847/1538-4357/ad58b9](https://doi.org/10.3847/1538-4357/ad58b9)
- Ji, Z., Alberts, S., Zhu, Y., et al. 2025, *ApJL*, 988, L69, doi: [10.3847/2041-8213/adf194](https://doi.org/10.3847/2041-8213/adf194)
- Kakiichi, K., & Gronke, M. 2021, *The Astrophysical Journal*, 908, 30, doi: [10.3847/1538-4357/abc2d9](https://doi.org/10.3847/1538-4357/abc2d9)
- Kakiichi, K., Ellis, R. S., Laporte, N., et al. 2018, *MNRAS*, 479, 43, doi: [10.1093/mnras/sty1318](https://doi.org/10.1093/mnras/sty1318)
- Kennicutt, Jr., R. C. 1998, *ARA&A*, 36, 189, doi: [10.1146/annurev.astro.36.1.189](https://doi.org/10.1146/annurev.astro.36.1.189)
- Kerutt, J., Oesch, P. A., Wisotzki, L., et al. 2024, *A&A*, 684, A42, doi: [10.1051/0004-6361/202346656](https://doi.org/10.1051/0004-6361/202346656)
- Kimm, T., & Cen, R. 2014, *ApJ*, 788, 121, doi: [10.1088/0004-637X/788/2/121](https://doi.org/10.1088/0004-637X/788/2/121)
- Koekemoer, A. M., Faber, S. M., Ferguson, H. C., et al. 2011, *ApJS*, 197, 36, doi: [10.1088/0067-0049/197/2/36](https://doi.org/10.1088/0067-0049/197/2/36)
- Komarova, L., Oey, M. S., Marques-Chaves, R., et al. 2025, *ApJ*, 994, 192, doi: [10.3847/1538-4357/ae0e0a](https://doi.org/10.3847/1538-4357/ae0e0a)
- Kron, R. G. 1980, *ApJS*, 43, 305, doi: [10.1086/190669](https://doi.org/10.1086/190669)
- Le Reste, A., Scarlata, C., Hayes, M. J., et al. 2025, *ApJS*, 280, 27, doi: [10.3847/1538-4365/adf227](https://doi.org/10.3847/1538-4365/adf227)
- Leclercq, F., Bacon, R., Wisotzki, L., et al. 2017, *A&A*, 608, A8, doi: [10.1051/0004-6361/201731480](https://doi.org/10.1051/0004-6361/201731480)
- Llerena, M., Pentericci, L., Napolitano, L., et al. 2025, *A&A*, 698, A302, doi: [10.1051/0004-6361/202453251](https://doi.org/10.1051/0004-6361/202453251)
- Madau, P., Ferguson, H. C., Dickinson, M. E., et al. 1996, *MNRAS*, 283, 1388, doi: [10.1093/mnras/283.4.1388](https://doi.org/10.1093/mnras/283.4.1388)
- Maji, M., Verhamme, A., Rosdahl, J., et al. 2022, *A&A*, 663, A66, doi: [10.1051/0004-6361/202142740](https://doi.org/10.1051/0004-6361/202142740)
- Markov, V., Bradač, M., Estrada-Carpenter, V., et al. 2025, *arXiv e-prints*, arXiv:2512.13778, doi: [10.48550/arXiv.2512.13778](https://doi.org/10.48550/arXiv.2512.13778)
- Mary, D., Bacon, R., Conseil, S., Piqueras, L., & Schutz, A. 2020, *A&A*, 635, A194, doi: [10.1051/0004-6361/201937001](https://doi.org/10.1051/0004-6361/201937001)
- Mas-Hesse, J. M., Kunth, D., Tenorio-Tagle, G., et al. 2003, *ApJ*, 598, 858, doi: [10.1086/379116](https://doi.org/10.1086/379116)
- Menon, S. H., Burkhart, B., Somerville, R. S., Thompson, T. A., & Sternberg, A. 2025, *ApJ*, 987, 12, doi: [10.3847/1538-4357/add2f9](https://doi.org/10.3847/1538-4357/add2f9)
- Meštrić, U., Vanzella, E., Beckett, A., et al. 2025, *A&A*, 698, A203, doi: [10.1051/0004-6361/202451959](https://doi.org/10.1051/0004-6361/202451959)
- Naidu, R. P., Tacchella, S., Mason, C. A., et al. 2020, *ApJ*, 892, 109, doi: [10.3847/1538-4357/ab7cc9](https://doi.org/10.3847/1538-4357/ab7cc9)
- Nedkova, K. V., Rafelski, M., Teplitz, H. I., et al. 2024, *ApJ*, 970, 188, doi: [10.3847/1538-4357/ad4ede](https://doi.org/10.3847/1538-4357/ad4ede)
- Oesch, P. A., Montes, M., Reddy, N., et al. 2018, *ApJS*, 237, 12, doi: [10.3847/1538-4365/aacb30](https://doi.org/10.3847/1538-4365/aacb30)
- Oke, J. B., & Gunn, J. E. 1983, *ApJ*, 266, 713, doi: [10.1086/160817](https://doi.org/10.1086/160817)
- Osterbrock, D. E. 1974, *Astrophysics of gaseous nebulae*
- Pahl, A., Topping, M. W., Shapley, A., et al. 2025, *ApJ*, 981, 134, doi: [10.3847/1538-4357/adb1ab](https://doi.org/10.3847/1538-4357/adb1ab)
- Pahl, A. J., Shapley, A., Steidel, C. C., Chen, Y., & Reddy, N. A. 2021, *MNRAS*, 505, 2447, doi: [10.1093/mnras/stab1374](https://doi.org/10.1093/mnras/stab1374)
- Peng, C. Y., Ho, L. C., Impey, C. D., & Rix, H.-W. 2002, *AJ*, 124, 266, doi: [10.1086/340952](https://doi.org/10.1086/340952)
- Peng, C. Y., Ho, L. C., Impey, C. D., & Rix, H.-W. 2010, *AJ*, 139, 2097, doi: [10.1088/0004-6256/139/6/2097](https://doi.org/10.1088/0004-6256/139/6/2097)
- Prichard, L. J., Rafelski, M., Cooke, J., et al. 2022, *ApJ*, 924, 14, doi: [10.3847/1538-4357/ac3004](https://doi.org/10.3847/1538-4357/ac3004)
- Puschnig, J., Hayes, M., Östlin, G., et al. 2017, *MNRAS*, 469, 3252, doi: [10.1093/mnras/stx951](https://doi.org/10.1093/mnras/stx951)
- Rafelski, M., Teplitz, H. I., Gardner, J. P., et al. 2015, *AJ*, 150, 31, doi: [10.1088/0004-6256/150/1/31](https://doi.org/10.1088/0004-6256/150/1/31)

- Rahner, D., Pellegrini, E. W., Glover, S. C. O., & Klessen, R. S. 2017, *MNRAS*, 470, 4453, doi: [10.1093/mnras/stx1532](https://doi.org/10.1093/mnras/stx1532)
- Rieke, M. J., Robertson, B., Tacchella, S., et al. 2023, *ApJS*, 269, 16, doi: [10.3847/1538-4365/acf44d](https://doi.org/10.3847/1538-4365/acf44d)
- Rivera-Thorsen, T. E., Hayes, M., & Melinder, J. 2022, *A&A*, 666, A145, doi: [10.1051/0004-6361/202243678](https://doi.org/10.1051/0004-6361/202243678)
- Rodriguez-Gomez, V., Genel, S., Vogelsberger, M., et al. 2015, *MNRAS*, 449, 49, doi: [10.1093/mnras/stv264](https://doi.org/10.1093/mnras/stv264)
- Rosdahl, J., Blaizot, J., Katz, H., et al. 2022, *Monthly Notices of the Royal Astronomical Society*, 515, 2386–2414, doi: [10.1093/mnras/stac1942](https://doi.org/10.1093/mnras/stac1942)
- Rudie, G. C., Steidel, C. C., Shapley, A. E., & Pettini, M. 2013, *ApJ*, 769, 146, doi: [10.1088/0004-637X/769/2/146](https://doi.org/10.1088/0004-637X/769/2/146)
- Rutkowski, M. J., Scarlata, C., Henry, A., et al. 2017, *ApJL*, 841, L27, doi: [10.3847/2041-8213/aa733b](https://doi.org/10.3847/2041-8213/aa733b)
- Saldana-Lopez, A., Hayes, M. J., Le Reste, A., et al. 2025, *arXiv e-prints*, arXiv:2504.07074, doi: [10.48550/arXiv.2504.07074](https://doi.org/10.48550/arXiv.2504.07074)
- Saxena, A., Cryer, E., Ellis, R. S., et al. 2022, *MNRAS*, 517, 1098, doi: [10.1093/mnras/stac2742](https://doi.org/10.1093/mnras/stac2742)
- Scarlata, C. M., Hu, W., Hayes, M. J., et al. 2025, *ApJ*, 985, 115, doi: [10.3847/1538-4357/adcf9a](https://doi.org/10.3847/1538-4357/adcf9a)
- Schaerer, D., Izotov, Y. I., Worseck, G., et al. 2022, *A&A*, 658, L11, doi: [10.1051/0004-6361/202243149](https://doi.org/10.1051/0004-6361/202243149)
- Shen, X., Vogelsberger, M., Boylan-Kolchin, M., Tacchella, S., & Kannan, R. 2023, *MNRAS*, 525, 3254, doi: [10.1093/mnras/stad2508](https://doi.org/10.1093/mnras/stad2508)
- Shibuya, T., Ouchi, M., Harikane, Y., & Nakajima, K. 2019, *ApJ*, 871, 164, doi: [10.3847/1538-4357/aaf64b](https://doi.org/10.3847/1538-4357/aaf64b)
- Siana, B., Teplitz, H. I., Colbert, J., et al. 2007, *ApJ*, 668, 62, doi: [10.1086/521185](https://doi.org/10.1086/521185)
- Simmonds, C., Tacchella, S., Maseda, M., et al. 2023, *Monthly Notices of the Royal Astronomical Society*, 523, 5468–5486, doi: [10.1093/mnras/stad1749](https://doi.org/10.1093/mnras/stad1749)
- Simmonds, C., Tacchella, S., Hainline, K., et al. 2024, *MNRAS*, 527, 6139, doi: [10.1093/mnras/stad3605](https://doi.org/10.1093/mnras/stad3605)
- Steidel, C. C., Bogosavljević, M., Shapley, A. E., et al. 2018, *ApJ*, 869, 123, doi: [10.3847/1538-4357/aaed28](https://doi.org/10.3847/1538-4357/aaed28)
- Steidel, C. C., Pettini, M., & Adelberger, K. L. 2001, *ApJ*, 546, 665, doi: [10.1086/318323](https://doi.org/10.1086/318323)
- Sun, G., Faucher-Giguère, C.-A., Hayward, C. C., et al. 2023, *ApJL*, 955, L35, doi: [10.3847/2041-8213/acf85a](https://doi.org/10.3847/2041-8213/acf85a)
- Sun, L., Wang, X., Teplitz, H. I., et al. 2024, *ApJ*, 972, 8, doi: [10.3847/1538-4357/ad5540](https://doi.org/10.3847/1538-4357/ad5540)
- Teplitz, H. I., Rafelski, M., Kurczynski, P., et al. 2013, *AJ*, 146, 159, doi: [10.1088/0004-6256/146/6/159](https://doi.org/10.1088/0004-6256/146/6/159)
- Trebitsch, M., Blaizot, J., Rosdahl, J., Devriendt, J., & Slyz, A. 2017, *MNRAS*, 470, 224, doi: [10.1093/mnras/stx1060](https://doi.org/10.1093/mnras/stx1060)
- Vanzella, E., Nonino, M., Cupani, G., et al. 2018, *MNRAS*, 476, L15, doi: [10.1093/mnrasl/sly023](https://doi.org/10.1093/mnrasl/sly023)
- Verhamme, A., Orlitová, I., Schaerer, D., & Hayes, M. 2015, *A&A*, 578, A7, doi: [10.1051/0004-6361/201423978](https://doi.org/10.1051/0004-6361/201423978)
- Verhamme, A., Orlitová, I., Schaerer, D., et al. 2017, *A&A*, 597, A13, doi: [10.1051/0004-6361/201629264](https://doi.org/10.1051/0004-6361/201629264)
- Wang, X., Teplitz, H. I., Smith, B. M., et al. 2025, *ApJ*, 980, 74, doi: [10.3847/1538-4357/ada4ab](https://doi.org/10.3847/1538-4357/ada4ab)
- Williams, C. C., Tacchella, S., Maseda, M. V., et al. 2023, *ApJS*, 268, 64, doi: [10.3847/1538-4365/acf130](https://doi.org/10.3847/1538-4365/acf130)
- Wisotzki, L., Bacon, R., Blaizot, J., et al. 2016, *A&A*, 587, A98, doi: [10.1051/0004-6361/201527384](https://doi.org/10.1051/0004-6361/201527384)
- Yajima, H., Umemura, M., Mori, M., & Nakamoto, T. 2009, *MNRAS*, 398, 715, doi: [10.1111/j.1365-2966.2009.15195.x](https://doi.org/10.1111/j.1365-2966.2009.15195.x)